Universiteit Utrecht

KWR Watercycle Research Institute

Assessment of the impact of ambient groundwater flow on High Temperature Aquifer Thermal Energy Storage (HT-ATES) performance and thermal spreading

MSc research Earth Sciences (GEO4-1520)

Faculty of Geosciences

Utrecht University

Utrecht, the Netherlands

In cooperation with:

KWR: Watercycle Research Institute

Nieuwegein, Netherlands

18 – 10 – 2019

Author	**Mark Diederen**	**3986179**
First supervisor	**dr. Niels Hartog**	**Utrecht University & KWR**
Second supervisor	**dr. Martin Bloemendal**	**TU Delft & KWR**

Abstract

High Temperature Aquifer Thermal Energy Storage (HT-ATES) is a technology where groundwater of up to 90 ˚C is stored in the subsurface which is used as a source of heat for spatial heating. By utilizing high temperatures, the use of a fossil-fuel heat pump as in low temperature (< 25˚C) ATES is excluded. Before realizing HT-ATES, a basic framework of the storage specific and site-specific hydrogeological conditions that effect the thermal recovery efficiency and thermal spreading of heat in the subsurface is needed. This study has provides a part of such framework by the hand of numerical simulations, specifically looking at the impact of ambient groundwater flow (AGF) on HT-ATES systems in scenarios with the presence of an overlying aquifer. Additionally, theoretical interpretations of the results help to explain the interaction between various processes modelled.

The results show that for HT-ATES systems in sites with ambient groundwater flow, thermal recovery efficiencies alter slightly due to the interaction between significant density-driven flow and ambient groundwater flow. However, the trend in ambient groundwater flow losses, where losses increase when decreasing the storage size or increase the AGF velocity, is similar to that of LT-ATES. Therefore, analysis whether *AGF* losses play a significant role at a certain site can still be performed with the analytical formula of Boemendal & Hartog 2018 that calculates efficiency losses due to ambient groundwater flow. In terms of spatial spreading, ambient groundwater flow causes for an increase in spreading in direction of the flow and increases when utilizing a larger storage aquifer. Additionally, flow in the storage aquifer results in more conduction losses to the overlying aquifer.

The presence of an overlying aquifer causes for an increase in thermal spreading in vertical direction when significant density driven flow is present. Density driven flow in the storage aquifer results in more heat to conduct upwards which then spreads vertically in the overlying aquifer as well due to density driven flow. Having flow in the overlying aquifer does not result in major losses in efficiency but does reduces the spreading vertically and increases it horizontally, causing a shift in spatial impact of the heat. Additionally, dispersion causes reduction of overall temperatures in the overlying aquifer, therefore decreasing the impact on the subsurface in terms of high temperatures. The insights of this study have provided a basic understanding of how HT-ATES interplays with site specific hydrogeological conditions and therefore how these must be taken into account when realizing HT-ATES.

Table of contents

List of parameters/symbols

Parameter	Symbol	Unit
Dynamic viscosity	μ	$N\ s/m^2$
Thermal retardation factor	R	-
Thermal radius	R_{th}	m
Hydraulic radius	R_h	m
Temperature	T	K
Time step	t	yr
Ambient groundwater flow velocity	u	m/yr
Flow velocity of groundwater	v	m/yr
Total injected storage volume per year	V_{inj}	m^3
Velocity of the thermal front	u^*	m/yr
Porosity	n	-
Well screen length	L	m
Injection volume	Q	m^3
Thermal conductivity water	k_{Tw}	$W/m/K$
Thermal conductivity of aquitards	k_{Taqt}	$W/m/K$
Thermal conductivity of aquifers	k_{Taq}	$W/m/K$
Vertical/horizontal hydraulic conductivity	k_v , k_h	m/yr
Water density	ρ_w	kg/m^3
Volumetric heat capacity water	c_w	$J/m^3/K$
Volumetric heat capacity aquifer	c_{aq}	$J/m^3/K$
Overlying aquifer thickness	H_{ov}	m
Storage aquifer thickness	H_{aq}	m
Energy in specific ground layer	E_{gl}	J
Density	ρ	kg/m^3

1. Introduction

Enhanced global warming has brought a heightened sense of urgency to transform the energy market towards a more sustainable sector. To reduce global greenhouse gas emissions, governments and companies set goals to accelerate a concerted transition in energy production and storage (UN, 2015; Ministry-of-Economic-affairs, 2016; TNO, 2018). Urban space heating and cooling is responsible for 40% of the world's energy consumption of which most is in the form of fossil fuels (RHC, 2013). A reduction in fossil fuel dependency in this sector may be achieved by the use of Aquifer Thermal Energy Storage (ATES) systems. The technique is seen as a possible gap closer between periods of high energy demand and high energy supply often caused by seasonal discrepancies (Fleuchaus, Godschalk, Stober, & Blum, 2018). Worldwide, the technique has a high potential in regions with convenient geohydrological conditions (Bloemendal, Olsthoorn, & van de Ven, 2015) and is suitable particularly for spatially large sites (e.g. office buildings, schools and shopping centers) because of its large site requirements (Hasnain, 1998).

Currently, low temperature ATES systems (LT-ATES) where the groundwater temperatures do not exceed 25˚C, are widely used (Fleuchaus et al., 2018). To utilize such water for the heating of well insulated buildings, a heat pump is required (Hesaraki, Holmberg, & Haghighat, 2015). For the heating process, the energy storage capacity and overall energy efficiency would increase if the use of high temperature (e.g. >60 ˚C) aquifer thermal energy storage (HT-ATES) systems would be applied in today's heating networks (e.g. Kabus, & Seibt, 2000; Sanner et al., 2005; Réveillère et al., 2013). A vast number of sectors, such as geothermal energy, solar energy or industrial waste heat, are seen as suitable energy sources (Wesselink, Liu, Koornneef, & van den Broek, 2018) and are capable to facilitate HT-ATES systems with sufficient energy. However, the economic feasibility for HT-ATES systems strongly depends on the recovery efficiency, which is relatively low compared to LT-ATES systems due to the occurrence of density-dependent flow (e.g. Mathey, 1977; Palmer et al., 1992; Molz et al., 1979).

The performance of an HT-ATES system is governed by the amount of energy loss as a consequence of several processes. Doughtly et al. (1982) described the related processes as dispersion, thermal conduction, density-driven flow and regional/ambient groundwater flow. Thermal conduction and dispersion cause the exchange of heat towards the surrounding subsurface, spreading the heat over a bigger area (Doughty, Hellström, Tsang, & Claesson, 1982). Density-driven flow is triggered by a difference in density between the hot injected water and the cold ambient water, resulting in free thermal convection which is expressed in upward flow of the hot water and tilting of the initially horizontal thermal front (Hellstrom, Tsang, & Claesson, 1979). Ambient groundwater flow results in displacement of the stored heat in direction of the flow (Bloemendal & Hartog, 2018). The significance of these processes in terms of efficiency loss is depending on operational factors (e.g. storage volume & temperature) as well as hydrogeological conditions (e.g. hydraulic conductivity). Doughtly et al. (1982) shows by a graphical method that the recovery efficiency of an ATES system can be determined. However, the presence of heterogeneity, buoyancy flow and ambient groundwater flow were neglected.

To a certain extent, the influence of the assumptions by Doughtly et al. (1982) have been studied. Heterogeneities in the aquifer distribute heat irregularly, but the influence on recovery efficiency is rather small and therefore can be, in most cases, neglected (Buscheck, Doughty, & Fu Tsang, 1983; Caljé, 2010; Ferguson, 2007; Sommer et al., 2015). Buoyancy flow is known to significantly lower recovery efficiencies when dealing both with high and low density differences (Buscheck 1983; Ward 2007; Drijvental 2012). Studies have quantified buoyancy flow in terms of loss in recovery efficiency or tilting of the thermal front (Hellström 1979; Ward 2007; Bakker 2010; Schout 2014). Additionally, measures that may counter buoyancy flow have been studied (Molz 1983; Lopik 2016). The influence of ambient groundwater flow is included in studies that estimate the performance of ASR and ATES systems in the Netherlands (Zuurbier 2013; Bloemendal 2018). Specifically for ATES systems, an analytical formula is determined that describes recovery efficiency loss due to ambient groundwater flow in the storage aquifer (Bloemendal & Hartog 2018).

With the eye on implementing HT-ATES into today's heating networks, it is key to have a basic understanding of how HT-ATES would perform in a setting with ambient groundwater flow. Preferably, systems would be realized in places with little to no ambient groundwater flow, but the reality is that ambient groundwater flow is present in the majority of places suitable for HT-ATES. Thus, having knowledge of the interaction between HT-ATES and ambient groundwater flow is crucial for realization of HT-ATES. Additionally, an aquifer above or beneath the utilized aquifer is commonly found in settings suitable for HT-ATES. Such aquifers have the

potential to increase spreading of the heat since heat that enters these aquifers would be able to experience density-driven flow, resulting in more vertical spreading. Furthermore, flow in these aquifers is expected to cause a significant decrease in recovery efficiency because of the constant supply of cold water at the horizontal cold/warm-water interface, keeping the temperature gradient relatively high, inducing higher thermal conduction rates in contrast with situations where no ambient groundwater flow is present. An overlying aquifer is considered to have a larger impact on the system since density-driven flow causes for upward flow of the heat, causing relatively more heat to enter an overlying aquifer compared to an underlying aquifer. Therefore, the presence of an overlying aquifer is examined in this study.

Besides a relatively more difficult heat recovery compared to LT-ATES, HT-ATES will leave a thermal footprint with overall higher temperatures in the subsurface. Concerns about the impact of LT-ATES systems on the overall water quality were already raised because of its potential to adversely affect other groundwater uses such as drinking water production (Hartog et al., 2013). A study showed that the small temperature differences ($\Delta T \leq 10$℃) where LT-ATES operates with does not significantly influence the concentrations of the main chemical constituents (Possemiers et al., 2014). However, due to the exponential temperature-dependence of both geochemical equilibria and rate constants, groundwater quality is expected to be more affected at high temperatures (Hartog et al., 2013). To reduce the risk of interference with surface activities, drinking water reserves or overall environmental impact, HT-ATES is typically realized in deeper aquifers (Wesselink et al., 2018). Having an idea of the thermal spreading of HT-ATES would provide knowledge about the scale of spatial influence that should be taken into account when realizing HT-ATES.

This research therefore attempted to provide an understanding of how HT-ATES systems would perform and behave in systems with ambient groundwater flow and an overlying aquifer. In doing such, the combination of density-driven flow, conduction and ambient groundwater is modelled and interpretations of the interaction between these processes is discussed. To frame the study, the research is divided in three scenarios where there is (a) ambient groundwater flow in the storage aquifer, (b) ambient groundwater flow in an overlying aquifer and (c) ambient groundwater flow in both aquifers. *Figure 1* gives a schematic overview of which processes would be present and discussed in the study.

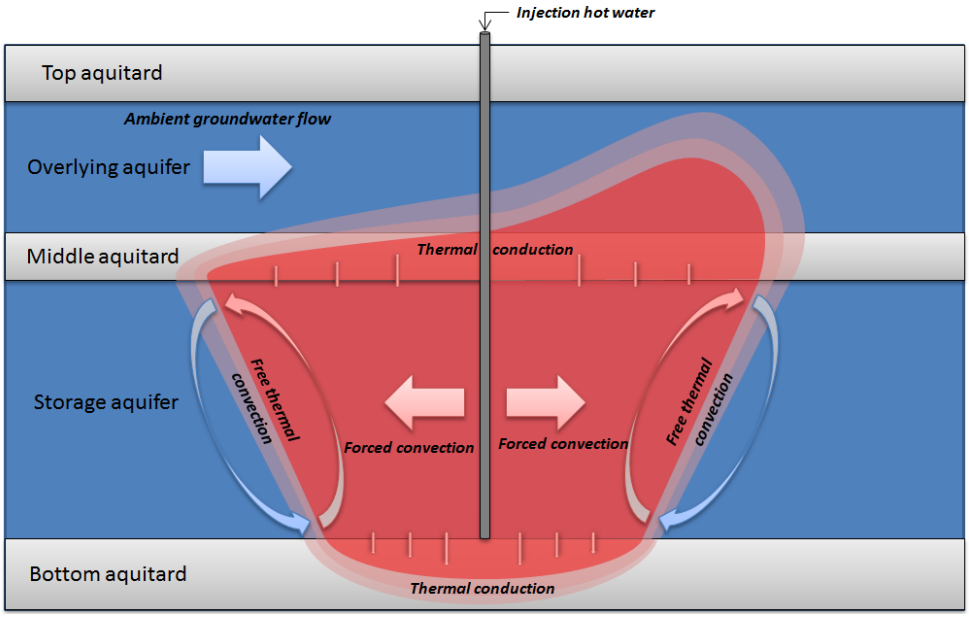

Figure 1 Schematic overview of the situation modelled in this study and the processes present with in this case ambient groundwater flow in the overlying aquifer. Note that the thicknesses of the layers do not correspond with the thickness of the layers modelled.

2. Methods

2.1 Theory

2.1.1 Thermal recovery efficiency

The amount of thermal energy that is recovered from the injected heat is referred to as the recovery efficiency (Doughty et al., 1982; Bloemendal 2018). By definition, recovery efficiency (η) is the ratio between the total amount of thermal energy recovered by extraction and the total amount of thermal energy stored by injection (E_{ext}/E_{inj}). The thermal energy can be written as $E = Q\Delta T\rho_w c_w$ where Q [m³] is the total volume of injected/extracted water, ΔT [°C] the difference in temperature between the injected/extracted water and the ambient groundwater, ρ_w [kg/m₃] the density of water and c_w [J/kg/°C] the specific heat capacity of water. The change in density and specific heat capacity of water at the used temperature range is neglected. Eventually the expression for recovery efficiency over a given time (often constructed of multiple storage cycles) is:

$$\eta(t_0 - t) = \frac{E_{ext,i}}{E_{inj,i}} = \frac{\int_{t_0}^{t} Q_{ext,i}\Delta T_{ext,i}dt}{\int_{t_0}^{t} Q_{inj,i}\Delta T_{inj,i}dt} = \frac{\Delta\bar{T}_{ext,i}V_{ext,i}}{\Delta\bar{T}_{inj,i}V_{inj,i}} \quad (1)$$

Where Q is the average discharge during time step t, and $\Delta\bar{T}$ the corrected temperature difference over time step t. In this study, the total injection and extraction volumes are equal ($V_{ext} = V_{inj}$) allowing comparison between the simulations. Additionally, the injected water temperature is constant to simplify the simulations.

2.1.2 Total energy per geological layer

To understand the difference in spreading of heat, the total energy per geological layer is calculated for each timestep. Knowing energy levels per layer allows to comprehend how the heat is distributed between the layers at a certain time step. By comparing energy levels between scenarios, an idea of the shift in spreading due to various processes can be obtained. The energy per layer is determined as follow:

$$E_{gl} = \sum E_z = \sum_{z_1}^{z_2} V_z c_b \Delta T_z \text{ at } t_{min} < t < t_{max} \quad (2)$$

Where E_{gl} is total energy [J] for a specific geological layer in the model which runs from the bottom of a layer (z_1) to the top (z_2), V_T is the volume of the subsurface with a temperature higher than the ambient groundwater temperature, c_b is the volumetric heat capacity of the bulk and ΔT is the difference in temperature between the measured temperature and the ambient groundwater temperature for each specific cell.

2.1.3 Mechanical dispersion and heat conduction

Initially, a sharp interface is present between the hot injected water and the ambient cold water. Mechanical dispersion and heat conduction cause the injected heat to spread over the interface. Thermal diffusion can be neglected because of its relatively little influence and due to the seasonal operation scheme (Anderson, 2005). The formula for effective thermal dispersion (D_{eff}) consists of a conduction and a dispersion term, each describing its relative effective contribution:

$$D_{eff} = \frac{k_{Taq}}{nc_w} + \frac{\alpha v}{n} \quad (3)$$

Heat conduction is represented by the first term, depending on the thermal conductivity of the aquifer (k_{Taq}), porosity (n) and the volumetric heat capacity of water (c_w). The rate of conduction can be determined with the increasing standard deviation $\sigma = \sqrt{2D_t t}$, with D_t being the right hand side of the effective thermal dispersion and (t) the time step [d]. A difference in properties between clay and sand causes a variation in the conduction term between the aquifers and aquitards. Assuming porosity and volumetric heat capacity to be constants of 0.3 and $4.2 \cdot 10^6$ [J/m³/K], the rate of thermal spreading over half a year is considered to be roughly 7 [m] in the aquifers, and 6 [m] in the aquitards due to conduction.

The second term describes the dispersion with (α) being the dispersivity, porosity (n) and (v) the velocity of the water, which is the sum of the forced convection induced by the well and the ambient groundwater flow (u). Assuming no flow in the aquitards that confine ATES systems atop and bottom, dispersion in these layers is neglectable. In the aquifers, depending on the velocity of the water, either conduction or dispersion is the dominant factor for the effective thermal dispersion. Frequently used dispersivities between 0.5-5 yield dispersion values of the same magnitude as conduction at flow velocities of 0.01-0.1 [m/d]. A study about

ATES systems in the Netherlands has concluded that even with high dispersivity rates of 5 m, conduction losses dominate after 10% of the storage volume is infiltrated (Bloemendal & Hartog 2018). Hence, dispersion losses are mainly present around the well during initial injection and final abstraction, while conduction losses are of importance further from the well.

2.1.4 Thermal retardation factor

Similar to a solute experiencing retardation caused by sorption, heat encounters thermal retardation due to the heat exchange between the water and the solid particles (Hecht-Méndez et al., 2010). Therefore, the thermal retardation factor (R) can be equivalently expressed in the heat transport equation as to how it is expressed in the solute transport equation. Its value depends on the ratio between the volumetric heat capacity of the aquifer and the volumetric heat capacity of water. The factor strongly influences the shape of the thermal volume with respect to ambient groundwater flow and forced convection flow.

$$R = \frac{\rho_{aq} c_{aq}}{n \rho_w c_w} \tag{4}$$

2.1.5 Shape of injection volume

Typically, injection is realized with a fully penetrating well in a confined aquifer, where no leakage through the aquitards is assumed (Doughty et al. 1973). By making this assumption, the storage volume may be visualized in a cylindrical shape, where the hydraulic radius (R_h) is defined as:

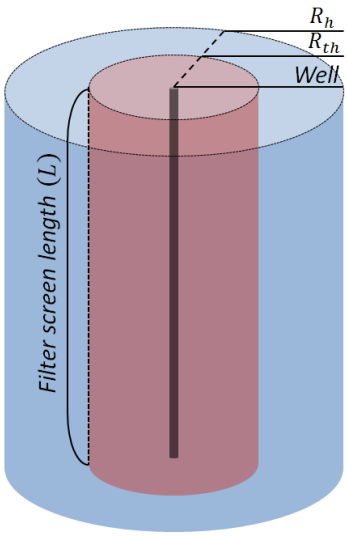

Figure 2 Hypothetical presentation of the hydraulic radius and the thermal radius for a fully penetrating confined system

$$R_h = \sqrt{\frac{V_{in}}{n \pi L}} \tag{5}$$

With the injection volume (V_{in}), porosity (n) and the screen length (L) (for a fully penetrating well). Losses in recovery efficiency will occur at the boundary of the thermal volume (*Figure 2*). Hence, the thermal radius (R_{th}) is of more interest and obtained by including the thermal retardation:

$$R\, \pi R_{th}^2\, nL = V_{in} \rightarrow R_{th} = \sqrt{\frac{V_{in}}{R \pi n L}} \rightarrow R_{th} = \sqrt{\frac{1}{R}} R_h \tag{6}$$

The stage of pumping operation determines the displacement of the thermal radius, tilting and spreading of the heat around the interface. During infiltration, high water velocities cause the displacement of the thermal front to be dominated by advective processes, bringing dispersion and conduction losses to a minimum. The hot-cold interface stays sharp because of the injected heat travelling faster than the standard deviation for the conduction. During storage, heat conduction and free thermal convection cause the heat to disperse over a larger area and the initial front to tilt. In the process of extraction, a combination of conduction and the opposite of the infiltration mechanisms will cause the heat to stay behind and spread over the initially stored heat volume. As a result, the lagged heat will cause recovery efficiencies in upcoming years to improve and stabilize over multiple storage cycles (Doughty et al. 1982).

2.1.6 Conduction and dispersion losses

Studies have shown that conduction losses can be minimized by optimizing the relation between area and volume of the stored heat. Doughty et al. 1982 took different hydrogeological properties for sand and clay layers into account and looked at the optimal ratio between well screen length and thermal radius (L/R_{th}):

$$\frac{L}{R_{th}} = \sqrt{\frac{C_{aq}\pi L^3}{C_w V_h}} \tag{7}$$

According to Doughty et al. 1982, the optimal L/R_{th}-ratio for low temperature storage is 1.5 [-]. Bloemendal & Hartog 2018 examined optimal screen lengths by looking at the ratio between thermal area and volume:

$$\frac{A}{V} = \frac{2\pi R_{th}^2 + 2\pi R_{th} L}{\pi R_{th}^2 L} = \frac{2}{L} + \frac{2}{R_{th}} \tag{8}$$

With the assumption that the lowest conduction losses are produced when the A/V-ratio is minimal, the optimal well screen length for a specific volume can be calculated with $L = 1.23\sqrt[3]{V}$.

The A/V-ratio shows the relation between efficiency losses and conduction and dispersion, where a higher A/V-ratio results in relatively higher conduction losses. It accounts for the conduction and dispersion losses at two sides of the spectrum, showing that for small aquifers thicknesses, the A/V-ratio changes relatively little when changing between large volumes, leading to minimal differences in conduction losses, whereas for large aquifer thicknesses, a variation in volume causes major changes in A/V-ratio and therefore conduction and dispersion losses. Previous studies have analysed the A/V-ratio and found that there is an optimum, where the lowest area over volume is present, which corresponds with the lowest losses in efficiency. Combining this with the optimal relation of Doughty et al.1982 that accounts for different thermal properties, the formula for optimal well screen length becomes $L = 1.02\sqrt[3]{V}$, resulting in smaller screen lengths.

2.1.7 Loss by ambient groundwater flow in HT-ATES systems

The retardation of heat induced by ambient groundwater flow can be calculated by dividing the ambient flow by the thermal retardation factor:

$$u_* = \frac{1}{R}u \tag{9}$$

Generally, the heat transport velocity is roughly half of the ambient groundwater velocity. Bloemendal & Hartog, 2018 investigated the effect of ambient groundwater flow on thermal recovery efficiency by studying LT-ATES systems in practice, located in areas with ambient groundwater flow. Combining geometrical laws with hydrological parameters, they produced an analytical formula that gives the thermal recovery efficiency (η_{th}) after losses due to ambient groundwater flow in the storage aquifer:

$$\eta_{th} = \frac{2}{\pi} a\cos\left(\frac{t_{sp}u_*}{2R_{th}}\right) - \frac{t_{sp}u_*}{\pi R_{th}^2}\sqrt{R_{th}^2 - \frac{1}{4}(t_{sp}u^*)^2} \tag{10}$$

The relation depends on the ambient thermal flow velocity (u_*), length of the storage period (t_{sp}) and thermal radius (R_{th}). The formula is based on the assumption that the injected volume of water preserves its cylindrical shape during displacement. This assumption is valid when no significant density-driven flow is present that tilts the thermal front and when ambient groundwater flow does not change the horizontal shape of the volume of a circle towards an ellipse (Bloemendal & Hartog, 2018; Ceric & Haitjema, 2005). Furthermore, the formula assumes horizontal displacement of heat with the R_{th} remaining a sharp interface between hot and cold water. Therefore, processes that cause for vertical heat displacement, such as density-driven flow, conduction and dispersion, are not considered and not accounted for.

2.1.8 Density driven flow

In groundwater systems, the displacement of fluid can be a result of a density gradient, referred to as 'free convection', or a hydraulic gradient, referred to as 'forced convection'. With HT-ATES, a difference in density between hot injected water and cold ambient groundwater causes upward flow of hot water and rotation of the initially vertical thermal front, eventually locating a considerable amount of hot water at the top of the aquifer (Doughty et al., 1982; Hellstrom et al., 1979). Additionally, the viscosity of water decreases at higher temperatures, enhancing density-driven flow (Hellstrom et al., 1979). The shape of the thermal volume becomes more of a cut-off cone structure, rather than a cylinder, causing cold water to be extracted at the bottom of the aquifer and hot water to be left at the top of the aquifer at the last part of the extraction period. This results in lower recovery efficiencies compared to systems with little to no density driven flow. Note that previous studies about conduction, dispersion and ambient groundwater flow assumed the storage volume to be of cylindrical shape. This assumption becomes less straightforward when considering significant density-driven flow.

The thermal front rotation has been studied by Hellström & Tsang 1979, whom derived the equation for the characteristic tilting time:

$$t_0 = \frac{H}{\sqrt{k_a^h . k_a^v}} \frac{C_a}{C_w} \cdot \frac{\pi^2(\mu_a + \mu_i)}{32.G.(\rho_a - \rho_i).g} \tag{11}$$

Where the aquifer thickness is given by H [m] , the horizontal and vertical aquifer permeability k_a^v and k_a^h [m^2], volumetric heat capacities of aquifer and water C_a and C_w [J/m3/K], μ_a and μ_i the dynamic viscosities of the ambient and injected water, ρ_a and ρ_i the densities [kg/m^3], G the Catalan's constant and g the acceleration of gravity (9.81 m/s^2). The equation gives an indication of which parameters are of importance for the tilting of the thermal front during free conduction.

Subsequently, studies have investigated the interplay between forced and free convection, which could either increase or decrease the angle of tilt. Hellström et al. 1979 discussed how the viscosity differences between hot and cold water can significantly enhance or reduce the density-driven tilting. Doughty et al. 1982 discussed that the diffusion of the thermal front, which results in a wider mixing zone and a smaller density gradient, results in a reduction of thermal front tilting. Studies about ASR, where fresh water with a lower density is injected in salt water bodies, showed that in cases where advection is predominant over density dependent flow, tilting of the thermal front is relatively little (Ward et al. 2007). The studies of Hellström et al. 1979, Doughty et al 1982 and Ward et al. 2007 should be taken in mind since this study considers high temperature storage with various pumping rates with the addition of ambient groundwater flow.

2.1.9 Overlying aquifers

Other than the storage aquifer, surrounding aquifers can cause additional losses in HT-ATES systems. The upward movement of heat makes it interesting to look at an overlying aquifer. The hydrogeological properties of an aquifer are often more favourable for the spreading of heat than aquitards since the thermal diffusivity in aquifers is generally higher and flow allows the presence of ambient groundwater flow and density driven flow. Ambient groundwater flow in an overlying aquifer can result in higher conduction gradients through the middle aquitard due to the inflow of cold groundwater at the bottom of the overlying aquifer.

Particularly ambient groundwater flow has the potential to induce higher conduction rates in upward direction and spreading heat over a larger area. Adding flow in such an aquifer could result in higher conduction gradients and therefore more losses.

2.2 Model setup

2.2.1 Numerical modeling

In order to evaluate the combined effect of dispersion, conduction and ambient groundwater flow on thermal recovery efficiency, a numerical model that solves the groundwater flow and heat transport equations simultaneously is required. Therefore, a model framework of Bloemendal 2018 that combines the hydrogeological code MODFLOW (Harbaugh et al., 2000) with the transport code MT3DMS (Hecht-Mendez et al., 2010; Zheng & Weng, 1999) is used. The two codes are combined in SEAWATv4 which models three-dimensional, saturated variable-density flow. Modeling heat transport with MT3DMS is allowed by treating the hot water as a solute that changes in concentration and density at higher temperatures. The differential equations in the model are solved by using the finite-difference method, allowing the simulation of hot water injection and extraction, as well as the occurrence of ambient groundwater flow (Bonte, 2013; Caljé, 2010; Sommer, 2015; Visser etal., 2015). For the solving of modflow, the PCG package was used because of its computational speed and no requirements of excessive memory. For the advective transport, the standard finite-difference method is used. The Python package 'Flopy' (Bakker et al., 2016) is used to produce and feed the parameters and initial conditions, run the model and visualize the results.

Parameter	Value	Unit
Horizontal conductivity aquifers	25	m/d
Horizontal conductivity aquitards	005	m/d
Hor./vrt. hydraulic conductivity	5	-
Longitudinal dispersion	1	m
Hor. transversal dispersion	0.1	m
Vert. transversal dispersion	0.01	m
Porosity	0.3	-
Bulk density	1890	kg/m3
Ambient groundwater temp.	12	C˚
Thermal diffusivity aquifer	0.127	m2/d
Thermal diffusivity aquitard	0.094	m2/d
Thermal distribution coefficient	2.0e-4	-
Specific heat capacity aquifer	1753	J/kg/K

Table 1 Modflow simulation parameter values

General properties of aquifers found in the Netherlands were used for the numerical modelling and can be found in Table 1 Modflow simulation parameter values(Calje 2010; Bloemendal & Hartog 2018). In order to answer the research questions, various scenarios are studied, where storage volume, temperature, ambient groundwater flow velocity and location of flow are altered (Table 2). The temperatures of 30-60-90 C˚ have been chosen according to expected temperatures to be injected in HT-ATES systems. The groundwater velocities are relatively high and chosen such that the results vary enough, allowing the analysis of the impact of ambient groundwater flow. The case with a storage volume of 400.000 m^3 and T_{inj} = 90 ˚C has been taken as the base scenario so that variations in volume in addition with significant density-driven flow can be observed. Additionally, several scenarios with no density-driven flow and no viscosity have been run in order to observe the additional influences of both processes and scenarios with a varying thickness of the middle clay layer in order to see the relevance of this thickness. Finally, scenarios with varying storage aquifer thicknesses, for the analysis of the A/V and L/Rth ratios were run.

Injection Volume [m^3/yr]	Injection Temp. [˚C]	agf. velocity [m/yr]	Presence of flow
100.000		0	
200.000	30	25	storage aquifer
400.000	60*	50	both aquifers
600.000	90	100	overlying aquifer
800.000			

Table 2 Overview of standard scenarios modelled in this study. Systems with an injection temperature of 60 ˚C were only modelled without flow

Although ATES systems commonly operate in pairs or multiple wells, to keep run times acceptable (<48 hrs), this study focuses on the efficiency and spatial impact around one well. The pumping regime of the well consists of a sinusoidal scheme. Generally this is seen as the best way to describe the peak of demand during winter and the peak of supply during summer (Oerlemans 2018, Bloemendal & Hartog 2018). The well is assumed to be a fully penetrating well, confined at the top and bottom of the storage aquifer. No thermal radiation from the well casing is assumed to be present.

2.2.2 Spatial & temporal discretization

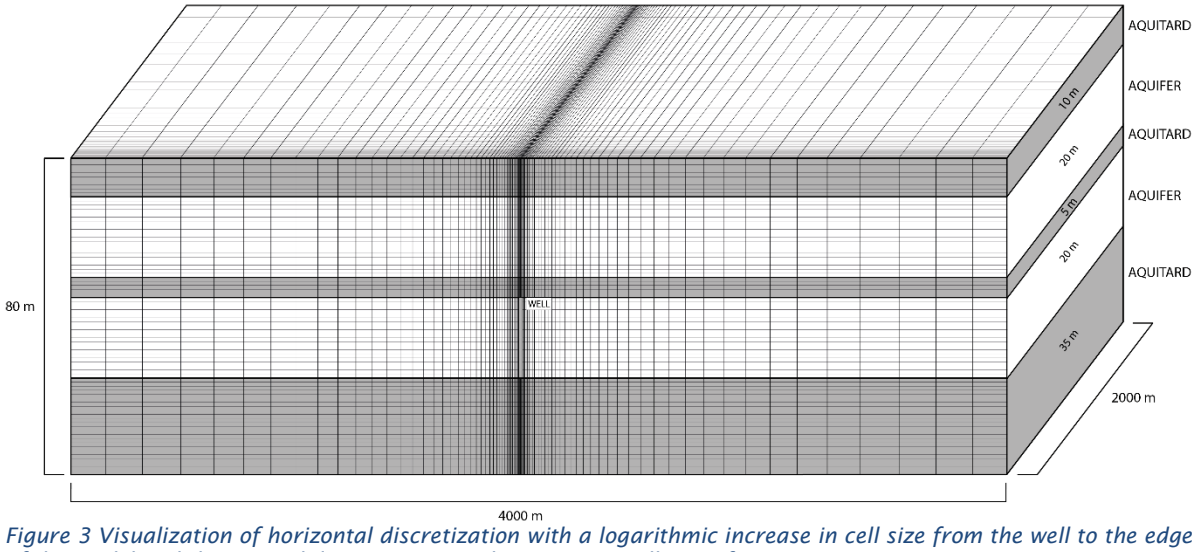

Figure 3 Visualization of horizontal discretization with a logarithmic increase in cell size from the well to the edge of the model and the vertical discretization with constant a cell size of 1 meter.

- Layering (*Figure 3*): The model has two aquifer and three aquitard layers, of which the upper, middle and bottom layer are aquitards that surround the aquifers (*Figure 1*). The thicknesses from top to bottom are consecutively 10, 20, 5, 20 and 25 meters. A relatively thin storage aquifer thickness compared to the storage volume is chosen, in order to minimize the tilting of the thermal front while still having realistic hydrogeological and operational settings. The top and bottom layer are set to constant head and temperature boundaries. The boundaries are assumed to be at a considerable distance since no difference in results were observed when having no temperature boundaries.

- Spatial discretization: Taking advantage of the plane symmetry in single well modelling with ambient groundwater flow, half a well with a reduction of 50% in pumping capacity is placed in a half domain-area of 2 by 4 kilometres, reducing the computational time (Maliva et al., 2006). In vertical direction, all cells have a size of 1 meter. In horizontal direction, the cells scale up logarithmically with a cell size of 3m at the well, ending with a cell size of 150 meter at 1550m from the well (*Figure 3*). The cells keep a size of 150m until the border at 2000m from the well. A sufficiently large model domain is chosen to assure the model boundary does not influence the outcomes. The discretization is tested with finer grid models, concluding that no significant numerical discretization occurs. Furthermore the model is well in line with models of other studies (Bloemendal 2018; Sommer 2014).

- Temporal discretization: Time steps of weeks are used with a total of 364 days within a year, resulting in 52 time steps per year with equal amount of injection and extraction steps. The time steps are chosen such that the pumping regime is in a smooth sinus form. The model iterates each cell within a time step until it has a courant number of <1. The model is run for 15 years in order to achieve a stabilized yearly recovery efficiency.

When running the model with this discretization and with a finer discretization, the difference in recovery efficiency is approximately 0.2%. Furthermore, when no ambient groundwater flow is present, steady state is reached after 10 to 15 years. Putting ICBUND at top and bottom does not influence the results of the model after 10 years. At and around the thermal front is considered to be the area of interest because of the processes we care about occurring most in this section. To minimize numerical dispersion and diffusion, the Peclet number in the mentioned part of the model is made sure to be *P<1*. Both the Courant and Peclet number are relatively high around the well, so numerical dispersion is likely to happen. However, although the cells are small and the flow is high, the numerical dispersion will not be of importance since the temperature around the well will generally stay the same.

2.2.3 Density

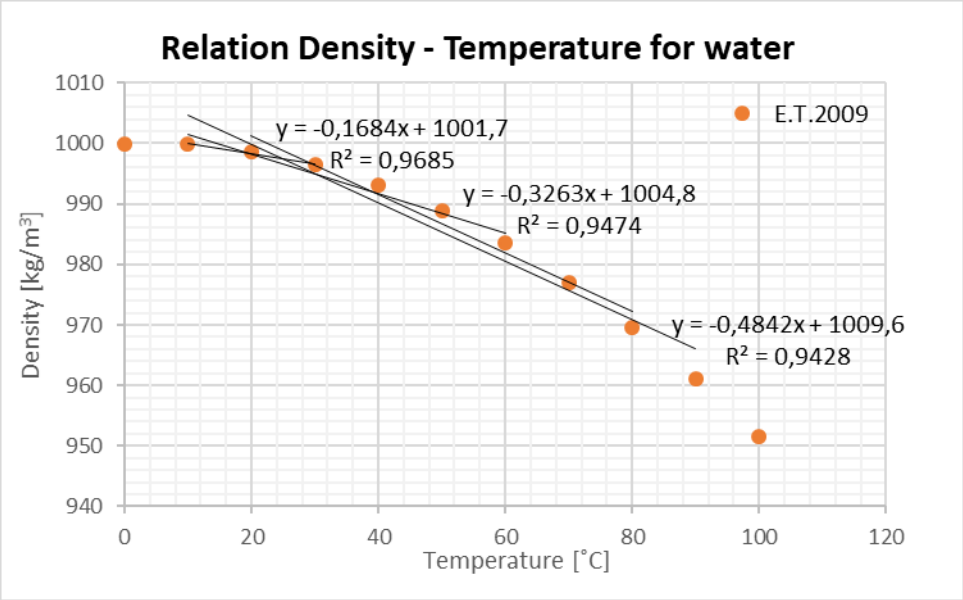

Figure 4 Change in density over temperature for fresh water. Three trend lines are added which represent the linear approximation for the three different temperature ranges modelled (12-30 ˚C, 12-60 ˚C and 12-90 ˚C). The slope of the corresponding trend line is used in MT3DMS for the $\Delta\rho_T$

The density of water decreases non-linearly over the temperature range of 12 to 90˚C used in the model (Engineering Toolbox 2009). The general trend shows that the change in density is smaller between 10 - 30˚C compared to the density change between 60 - 90˚C (*Figure 4*). Implementation of this non-linear relationship is key to the modelling of density-driven flow. However, in SEAWAT, the density can only be coupled to temperature with a linear relationship. Therefore, an approximation of the linear trend over the temperature range used in a run is made. Because of the usage of three different temperature ranges (12-30˚C, 12-60˚C and 12-90˚C), a linear trend for each temperature range is produced. The density gradient obtained from the trend is used when modelling the corresponding temperature range. All linear configurations show a high value for R^2, indicating that the usage of a linear approximation for density driven flow is acceptable.

2.2.4 Viscosity

The viscosity of water decreases with an increase in temperature, making it less viscous and therefore enhancing the flow velocity. Our model neglects all chemical components in the water and calculates the dynamic viscosity only based on water temperature. The formula used for this originates from Dierch & Kolditz, 2002, and the constant values that relate the dynamic viscosity with temperature are from Voss 1984, giving:

$$\mu(T) = 239.4 \times 10^{-7} \cdot 10^{\left(\frac{248.37}{T+133.15}\right)} \quad (12)$$

2.2.5 Analysis of the numerical data

Regarding this studies results, efficiency is studied by analysing the recovery efficiencies from the modelled scenarios. In all cases except for the model validation, the recovery efficiency produced over the last year of operation (year 15), is used for the analysis. Reason is that the recovery of last year is closest to the constant recovery efficiency that the system eventually will reach in steady state.

In order to analyse the horizontal thermal spreading of the system, the distance travelled by water of 13 ˚C, 15˚C and 51˚C is observed. The spreading is measured at the top of the storage aquifer and at the bottom of the overlying aquifer. The top of the storage aquifer has been chosen because the tilting of the thermal front due to density-driven flow will lead to most horizontal spreading in this plane. The bottom of the overlying aquifer is chosen because it being the boundary towards the storage aquifer. Spreading in this plane will give an idea how much vertically conducted heat will spread horizontally in the overlying aquifer and how various flow regimes effect the thermal conduction between the two aquifers.

3. Results

3.1 Model validation

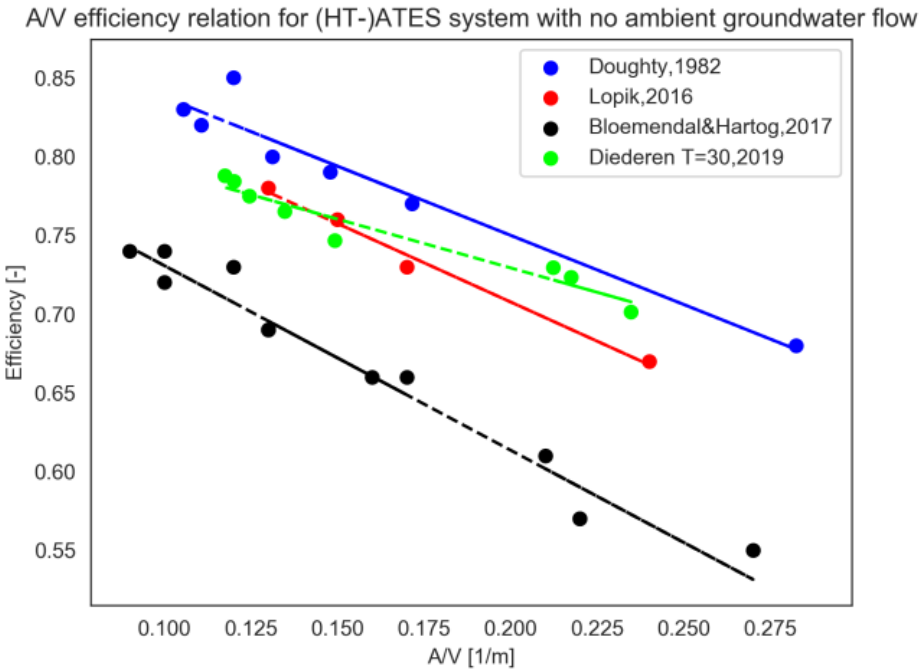

Figure 5 Efficiencies of low temperature (T_{inj} = 30 ˚C) scenarios modelled without ambient groundwater flow versus Area over volume (A/V) of each corresponding system. Additionally the efficiencies of other studies have been added to compare the trend for model validation.

To validate the model, the recovery efficiencies of cases with low injection temperatures (T_{inj}=30 ˚C) were compared with those of previous performed studies where density-driven flow was neglected (*Figure 5* Efficiencies of low temperature (Tinj = 30 ˚C) scenarios modelled without ambient groundwater flow versus Area over volume (A/V) of each corresponding system. Additionally the efficiencies of other studies have been added to compare the trend for model validation.). The low A/V-values show the same trend as the other studies. The higher A/V scenarios cause a decrease in slope of the trend line. The efficiencies of the higher A/V-values are higher because of the scenarios being modelled without an overlying aquifer. An overlying aquifer results in more vertical conduction due to the presence of flow and the lower thermal conductivity of an aquifer, relative to an aquitard. The scenarios were modelled without an overlying aquifer to keep run times acceptable (<3 days), however this resulted in higher efficiencies. The general difference in efficiencies between studies lies in the usage of varying hydrogeological, operational and spatial setups. Overall, taking the similar trend and the explanation for possible discrepancies in mind, the results give confidence in the validity of the numerical predicted recovery efficiencies.

3.2 HT-ATES systems in regions with no ambient groundwater flow

3.2.1 Analysis of HT-ATES systems performance without *AGF*

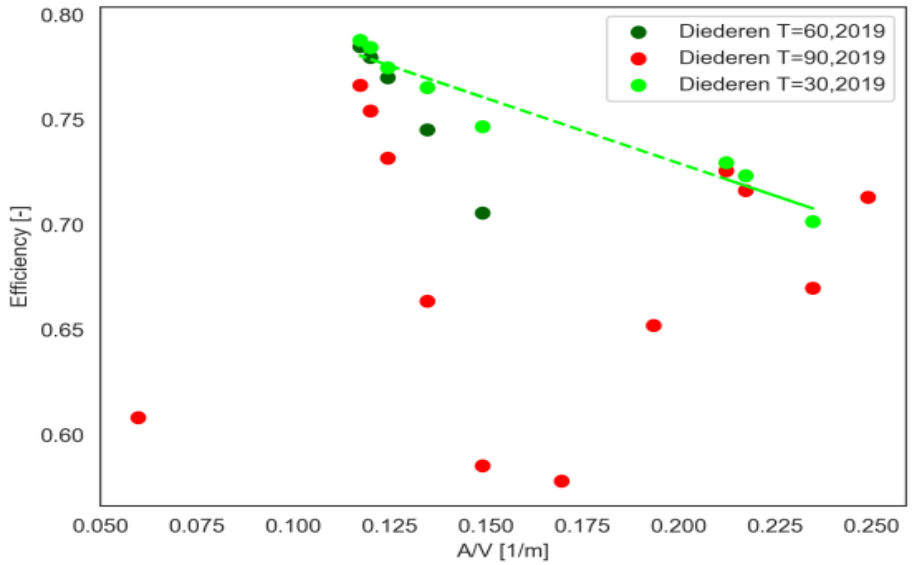

Figure 6 Simulated efficiencies over A/V for systems with different injection temperatures. Showing the loss in trend for high temperature storage.

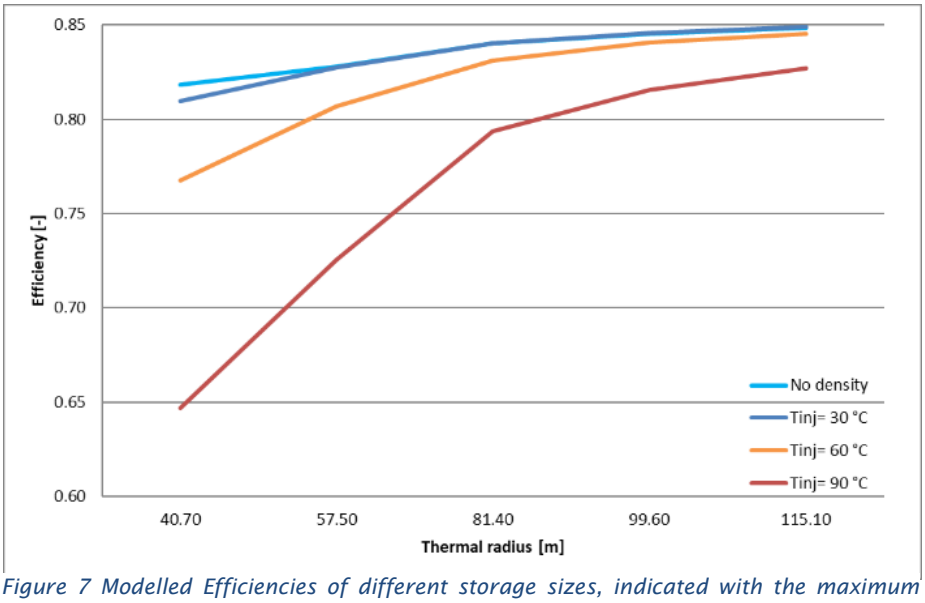

Figure 7 Modelled Efficiencies of different storage sizes, indicated with the maximum thermal radius, and different injection temperatures. The utilized storage aquifer thickness (H_{aq}) = 20 m

The recovery efficiencies of the modelled scenarios with $T_{inj} = 90℃$, $T_{inj} = 60℃$ and $T_{inj} = 30℃$ without ambient groundwater flow are presented as a function of A/V (*Figure 6*). Except for the results between 0.10 < A/V < 0.15 where the aquifer thickness is the same for each scenario, the difference between results with the same injection temperature (T_{inj}) are the storage volume (V_{str}) and the aquifer thickness (H_{aq}). The results of $T_{inj} = 90℃$ and the $T_{inj} = 30℃$ scenarios show that the utilization of a higher injection temperature (T_{inj}) results in a loss in trend over the A/V-ratio. The loss in trend makes sense when considering that the A/V ratio is rather a measure for conduction/dispersion losses and does not embody the thickness of the aquifer. Therefore, systems with varying aquifer thicknesses, resulting in different degrees of tilt, can have the same A/V-ratio when changing the storage volume. Since the amount of tilting influences the process of thermal recovery, scenarios with the same A/V-ratio can have varying recovery efficiencies, explaining the loss in trend.

Plotting the efficiencies of scenarios without ambient groundwater flow over the maximum thermal radius of the corresponding system (*Figure 7*) shows that when decreasing the maximum storage volume (V_{str}) of a system, the efficiency exponentially decreases when utilizing a high injection temperature. Additionally, the amount exponential decrease, increases when increasing the injection temperature. The similarity in efficiency between the $T_{inj} = 30$°C scenarios and the scenarios where no density is modelled indicates that the $T_{inj} = 30$°C scenarios experience little to no losses due to density driven flow.

The tilting of the thermal front increases when unitizing higher injection temperature, explaining the increase in losses due to a higher injection temperature. The increase in losses due to the use of a smaller storage volume can be explained by assuming that the tilting of the thermal front is relatively little for systems with the same injection temperature. The results of travelled distance of the contour line when adding density-driven flow (section 3.2.2b) agree with this assumption (*Figure 15*). *Figure 8* displays hypothetically the difference between a system with a large thermal radius and a small thermal radius in a scenario with rotation of the thermal front. Assuming the tilting of the thermal front to be constant for scenarios with the same injection temperature, the radial distance over which the tilting takes place (ΔR_{tf}) stays the same regardless of the storage volume. If the radial distance over which the tilting takes place (ΔR_{tf}) is large compared to the radial distance of the injected volume (R_{th}), a relatively large volume is lost at the circumference due to tilting. Since the required volume changes exponentially over thermal radius, the influence of the thermal front tilting increases exponentially in direction of a smaller thermal radius. Therefore, the efficiency decreases in the same manner when going to a smaller thermal radius. Since the exponential losses in efficiency are in line with this explanation, it is concluded that this relation between the tilted thermal front and the thermal volume is most important in affecting the recovery efficiency of the system.

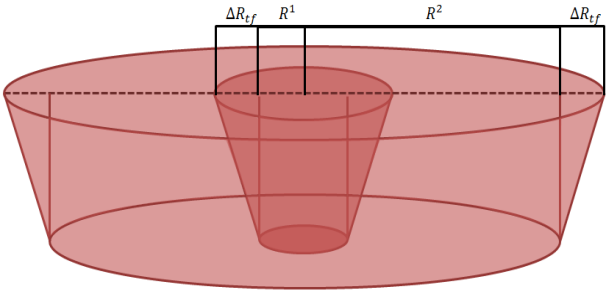

Figure 8 Hypothetical representation of the thermal storage volume of a HT-ATES, illustrating how the ratio between thermal radius and radius of tilting alters for different storage sizes.

3.2.2 Thermal geometry of HT-ATES systems in regions with no ambient groundwater flow

3.2.2a The effect of conduction & dispersion on thermal spreading

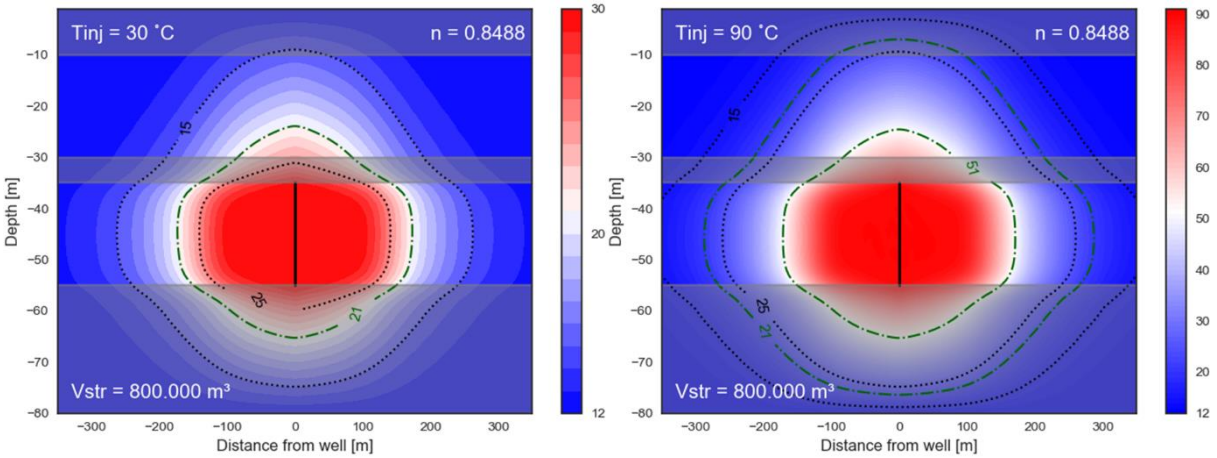

Figure 9 Two thermal cross sections with an injection temperature (T_{inj}) of 30 °C (left) and 90 °C (right). The cross sections are taken at the end of the last injection period (year 15, time step 740). Both scenarios are modelled without density driven flow and have a total storage volume of 800.000 m³. The contour lines of 15 °C, 21 °C, 25 °C and 51 °C are highlighted to enable the comparison between same temperature contours between the two scenarios.

To assess the thermal geometry due to conduction and dispersion, two no-density scenarios with $T_{inj} = 30$°C and $T_{inj} = 90$°C, with the same storage volume are presented (*Figure 9*). Both scenarios have the same recovery efficiency (*n = 0.8488*), indicating that when no density-driven flow is modelled, the relative efficiency of the system is independent of the injection temperature. The shape of the thermal volume in both scenarios is similar, indicating that the area over which the system influences the temperature is independent of the

injection temperature. However, comparing the highlighted contour lines of both cross sections shows that contour lines of the same temperature are displaced further from the well when having a higher injection temperature. Thus, a system with a higher injection temperature has a larger impact on the surrounding area.

The reason for both systems having a similar thermal geometry when no density driven flow is modelled is that a higher injection temperature does not change the effective dispersion coefficient (Eq. 3). However, the higher injection temperature does change the difference in temperature between the injected water and the ambient groundwater (ΔT). As a result, the overall dispersed heat increases, causing higher temperatures to reach further, impacting a larger area. The conduction/dispersion can be visualized with the function shown in *Figure 10*, where T_i is the initial temperature from the ambient groundwater, ΔT the difference in temperature between the ambient groundwater and the injected water and x the value given to the error function $erfc(x)$ which depends distance, time and the effective dispersion coefficient. The figure shows that a higher injection temperature, thus a higher ΔT, results in overall higher temperatures to spread over the same distance when distance, time and the effective dispersion coefficient are constant for both scenarios.

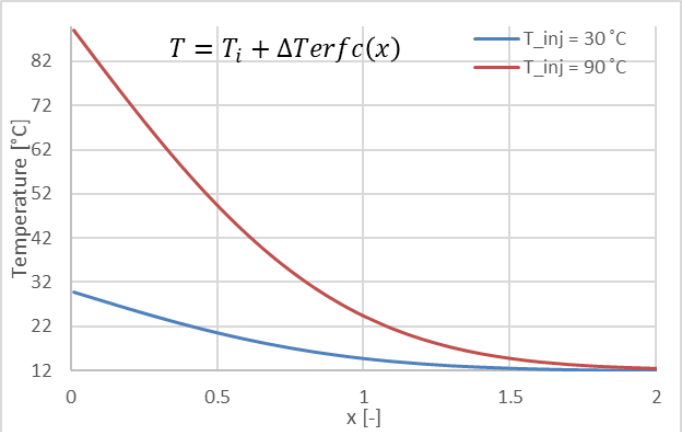

Figure 10 Visualization of temperature spreading due to conduction/dispersion over x, where x is the value fed to the error function, depending on space and time.??

3.2.2b The effect of viscosity on the tilting of the thermal front

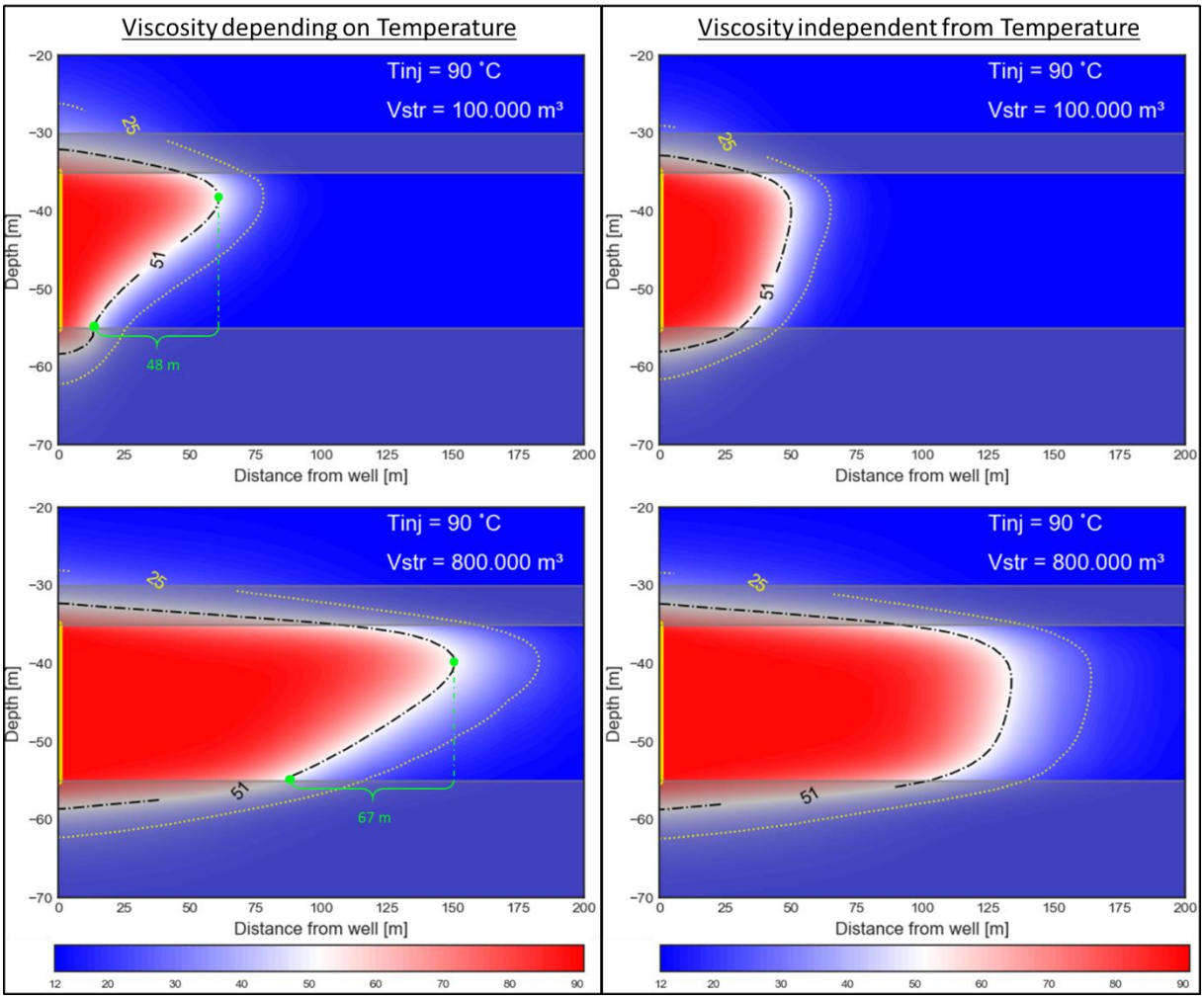

Figure 11 Vertical thermal cross-sections for scenarios with an injection temperature of 90°C, taken at the end of the first full injection period (t = 65, 1.25yr). The no-AGF scenarios are axisymmetric, therefore the cross-sections are taken from the well (gold vertical line at x=0m, -35m>Depth>-55m) onwards. Difference in scenarios presented are the storage volume, 100.000 m³ (upper) and 800.000 m³ (lower), and modeled with viscosity (left) and without viscosity (right). The contour lines of 25°C and 51°C are highlighted and the horizontal distance over which tilting of the thermal front took place in the scenarios with viscosity (left) are indicated. For the scenarios without viscosity, tilting was not significant and therefore not highlighted. Note that the figure is exaggerated in depth.

Considering the difference in horizontal flow rate, thermal cross-sections of the largest and smallest system modelled are presented to assess the impact and shape of the thermal volume of HT-ATES without AGF (*Figure 11*). The thermal cross-sections of the small system (*Figure 11 upper*) shows that heat in the storage aquifer reaches the furthest at a depth of $z \approx -38$ *m* as a result of the interaction between the cold middle aquitard and the thermal volume/front. For the larger system (*Figure 11 lower*), heat reaches the furthest slightly deeper ($z \approx -40$ *m)* because of a larger area of the cold middle aquitard interacting with the thermal front over the injection period. Additionally, comparing the highlighted temperature contours of the two storage sizes (*Figure 11*) shows that the large system *(V_{str} = 800.000 m²)* produces more spreading horizontally than the small system.

Comparing the scenarios where viscosity is either dependent or independent on temperature shows that viscosity has a significant role in tilting of the thermal front. When viscosity is independent from temperature, the tilting of the thermal front relatively the same, regardless of storage size (*Figure 11 right).* When viscosity depends on temperature, tilting of the thermal front significantly increases (*Figure 11 left*). Additionally, the distance over which tilting takes place is more for the larger system *(+19 meters*). The significant increase in tilting due to the temperature-viscosity relation and larger tilting for a larger system can be explained with the theory of Hellström 1979.

Hellström 1979 theory states that the enhanced tilting is an effect of the difference in viscosity between the hot water, experience less flow resistance, and the cold ambient groundwater, experiencing more flow resistance. Considering the operation of injection, the density difference causes the initial tilting of the thermal front. Subsequently, the horizontally flowing hot water at the middle and lower part of the storage aquifer is partly redirected upwards when reaching the thermal front because of the more viscous cold water acting as a hypothetical barrier *(Figure 12*). At the top of the storage aquifer, the cooling of the middle aquitard produces a viscosity difference at the intersect between the middle aquitard and the storage aquifer, resulting in a similar viscosity barrier that redirects the water downwards. The combination of both results in the thermal geometry of the thermal front seen in the results (*Figure 11*).

The increase in distance over which tilting takes place when the systems storage size is increased, is a result of a higher horizontal flow rate. Bearing in mind that the interval over which injection/extraction takes place is the same for each storage size modelled, the increase in storage size results in the thermal radius to experience higher horizontal flow rates over a larger distance, resulting in more cooling at the top of the thermal front and a longer distance over which the heat is partly redirected. The concave upward course of the 51 contour line at the end of the injection period is because of the low flow rate in horizontal direction in the last few time steps. Vertical flow starts to dominate, causing the concave upward course. For the large system, the horizontal flow rate at the thermal radius stays relatively dominant until the last time step of the injection period, causing the concave downwards course of the 51 contour. Overall, the results show the importance of modelling the combination of density and viscosity in HT-ATES systems.

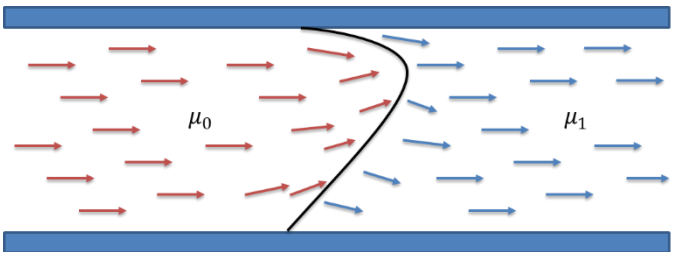

Figure 12 Hypothetical representation of the influence on horizontal flow when having a viscosity difference between the hot and cold water, resulting in the eventual shape of the thermal front.

3.2.2c Evolution of the thermal geometry over time

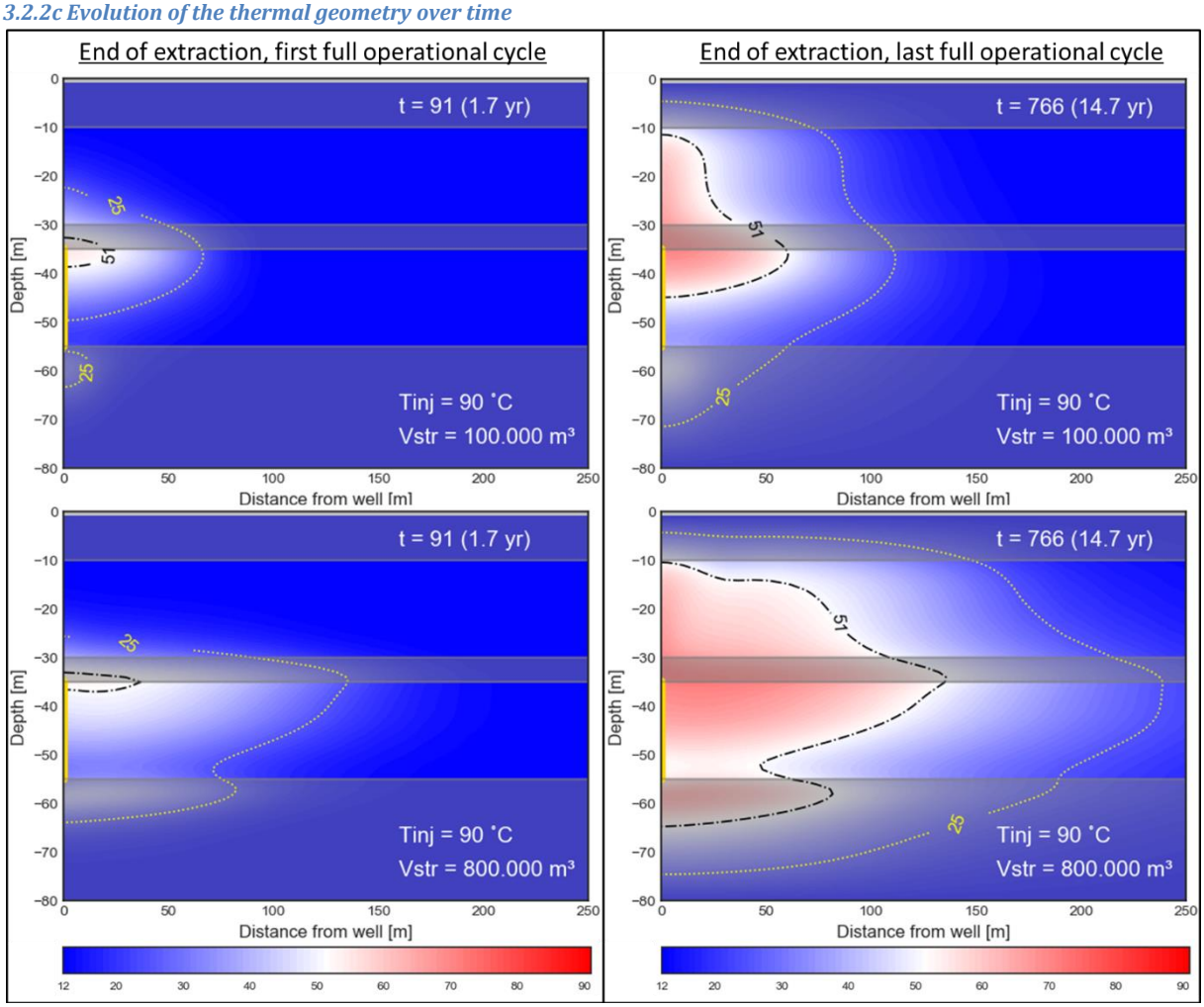

Figure 13 Vertical thermal cross-sections of scenarios with an injection temperature of 90°C, taken at the end of extraction after the first full operational cycle (t = 91, 1.7yr) (left) and the last full operational cycle (t = 766, 14.7 yr) (right) for systems with a storage volume of 100.000 m³ (upper) and 800.000 m³ (lower). The no-AGF scenarios are axisymmetric, therefore the cross-sections are taken from the well (gold vertical line at x=0m, -35m>Depth>-55m) onwards. The contour lines of 25°C and 51°C are highlighted.

Figure 13 illustrates the development of residual heat in the subsurface through time by presenting thermal cross-sections taken at the end of the extraction period after the first full operational cycle (t = 91, 1.7 yr) and the last full operational cycle (t = 766, 14.7 yr) of the smallest (V_{str} = *100.000 m³*) and largest (V_{str} = *800.000 m₃*) systems modelled. Assessment of the cross-sections after the first full operational cycle (*Figure 13 left*) shows that the larger system leaves more residual heat in the storage aquifer, in horizontal and vertical direction. Over time, this results in the large system leaving relatively more residual heat over the entire storage aquifer, whereas the smaller system leaves heat mainly in the top of the storage aquifer.

In both systems, a significant amount of heat accumulates at the top of the storage aquifer (*Figure 13 left*) resulting in much of the heat conduction towards the overlying aquifer (*Figure 13 right*). The smaller system conducts energy vertically further in the early stage of operation, whereas the spreading of heat over a larger area for the larger system results in a more widespread conductive pattern towards the overlying aquifer. Considering no flow in the middle aquitard, over time, the vertically conducted heat produces two distinctive patterns in the overlying aquifer. In both scenarios, the highest temperatures are situated above the well (*Figure 13 right*). The larger spreading in horizontal direction for the larger system creates a secondary heat circle. The boundary between the primary heat peak and the secondary heat circle is roughly at the same distance as where the heat accumulates at the end of first year extraction. Therefore it is assumed that this pattern is caused due to the tilting of the thermal front. Furthermore, the highlighted contour lines reach closely towards the top of the aquifer, indicating that interference with the constant temperature boundary at the top of the model is likely to occur. Overall, relatively large accumulation of residual heat in the overlying aquifer indicates that HT-ATES produces a significant increase in vertical heat displacement that should be considered.

3.2.2d Horizontal spreading of the thermal volume

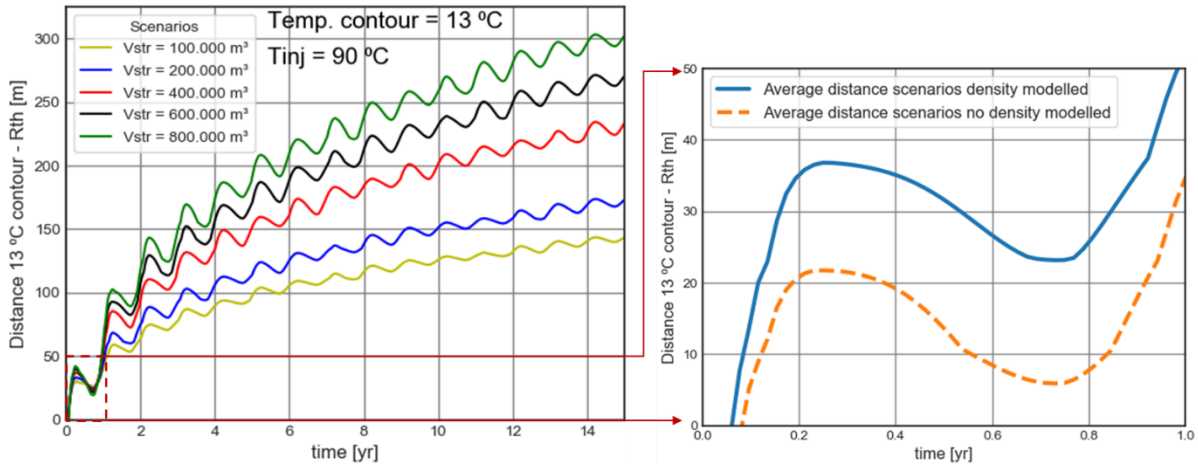

Figure 14 Course of the 13 ˚C contour line over time (0<t<15 yr) for T_{inj} = 90 ˚C scenarios with different storage sizes (V_{str}), measured at the top of the storage aquifer (z = -35 m) and starting with y = 0 at the thermal radius corresponding to the storage size (Left). The first year of operation is magnified and the average distance travelled by the 13 ˚C contour is plot together with the average distance travelled

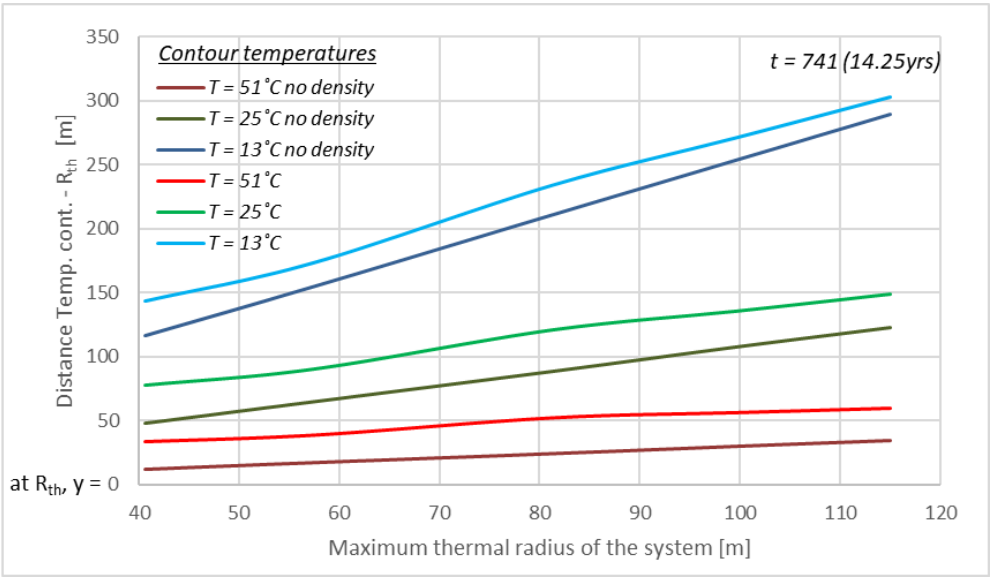

Figure 15 Distance from the 51 ˚C, 25 ˚C and 13 ˚C contour lines in horizontal direction, measured at the top of the storage aquifer (z = -35m), at the end of the last full injection period (t = 741, 14.25 yr). The y-axis is 0 meters at the thermal radius that corresponds with the maximum thermal radius of the system (for x = R_{th} = 50 m, y = 0 at R_{th} = 50 m). Presented are the T_{inj} = 90 ˚C scenarios modelled with and without density.

Horizontal spreading of the injected heat for T_{inj} = *90 ˚C* scenarios without ambient groundwater flow is assessed by examining the distances that the 51 ˚C, 25 ˚C and 13 ˚C temperatures have travelled over time (*Figure 14*) and where the temperatures are located at the end of the last full injection period (*t = 741, 14.25 yr*) (*Figure 15*). Heat moves the furthest between *-38 m* and *-40 m*, however, to enable comparison between different storage sizes and because of the direct contact with the middle aquitard, the top of the storage aquifer (*z = -35 m*) is chosen as the plane over which the horizontal spreading is measured. The distance travelled by the contours are measured starting with x=0 at the thermal radius (R_{th}) corresponding to the modelled storage size.

For each storage volume, the thermal spreading increases over time *(Figure 14*). The trend of each scenario shows that eventually the temperature would reach a maximum distance at which the system is in steady state for each operational year. However, steady state is not reached after 15 years since the overall distance still increases after last modelled year. The operation of injection/extraction translates in an oscillation pattern, where one cycle is completed over one year. The magnified part (*Figure 14 right*), with the average distance travelled by the 13 ˚C contour for scenarios with and without density-driven flow, shows that early in the first year (*t = ±0.1 yr*), scenarios with density driven flow have an increase in spreading of approximately 20-25 meters compared to scenarios without density-driven flow. After 14 years, at the end of the last full injection period (*Figure 15*), the distance between the 13 ˚C contour for scenarios with and without density-driven flow is still approximately 20-25 regardless of storage size, indicating that the additional effects of density-driven flow do not add up in spreading over time.

Figure 15 shows that this is also the case for the 51 ˚C and 25 ˚C contour, confirming that density-driven flow does not add significantly to temperature spreading. Additionally, *Figure 15* shows that, with respect to storage volume, the heat travels a further distance from the thermal radius when a larger volume is utilized, indicating that conduction/dispersion increases when a larger storage volume is used. To evaluate whether it is dispersion or conduction that causes the increase in spreading, the dispersion and conduction part of the effective dispersion coefficient (Eq. 3) are calculated for the largest and smallest system and given in appendix 2. Since conduction stays the same, the high dispersion coefficients of the larger system relative to those of the small system indicate that the large system experiences significantly more dispersion, resulting in the increase in spreading. Therefore, when realizing HT-ATES with a large storage volume that results in a relatively flat system, the increase in dispersion should be considered.

3.3 HT-ATES systems with ambient groundwater flow in the storage aquifer

3.3.1 Analysis of HT-ATES systems performance with *AGF* in the storage aquifer

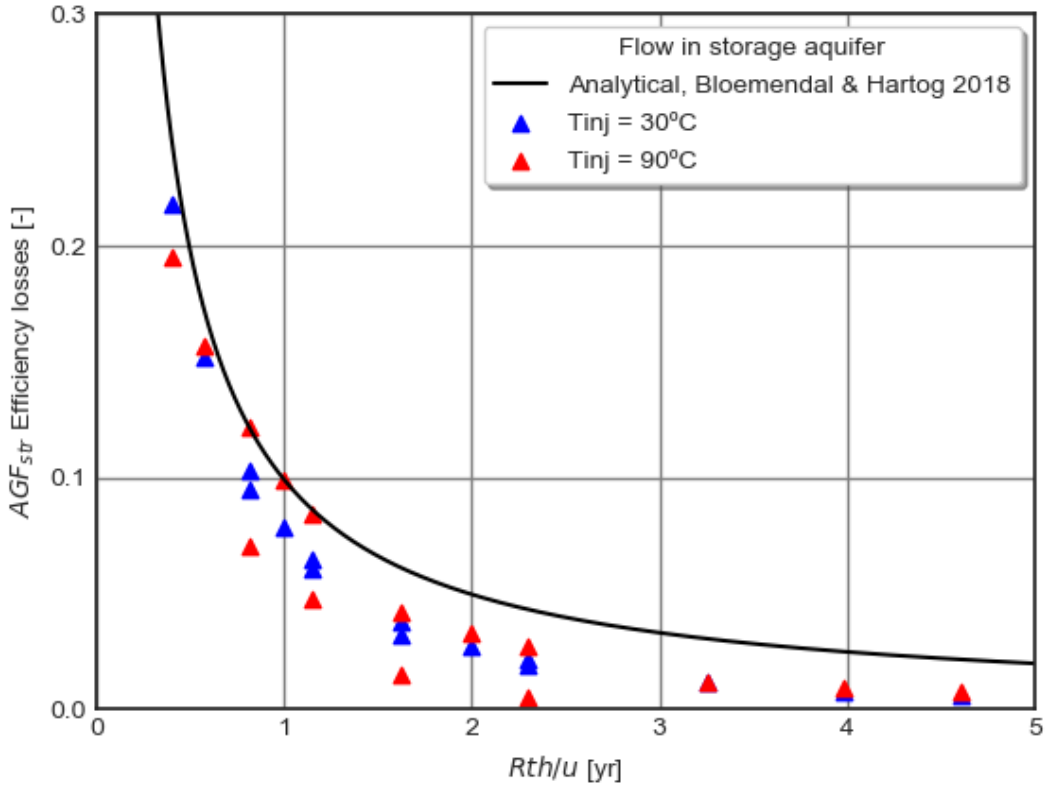

Figure 16 Relation between AGF_{str} efficiency losses and thermal radius over AGF velocity for the AGF_{str} numerical simulation results and the analytical formula for a storage period of 0.5 yr. For the scenarios modelled without density, three efficiencies are plot because only V_{str}=400.000 m^3 scenarios were modelled without density and AGF_{str}.

For scenarios with T_{inj} = 30˚C, T_{inj} = 90˚C and T_{inj} = 90˚C without density driven flow, the losses in re covery efficiency due to ambient groundwater flow in the storage aquifer (AGF_{str}), referred to as AGF_{str} efficiency losses, are obtained by looking at the difference in recovery efficiency between scenarios with AGF_{str} and without ambient groundwater flow (AGF_{no}). The AGF_{str} losses are plot over R_{th}/u together with the analytical formula from Bloemendal & Hartog 2018 (Eq.10) (*Figure 16)*. The analytical formula is added in terms of efficiency loss by subtracting the calculated efficiency from total efficiency.

For the low temperature scenarios (T_{inj} = 30 ˚C), the losses due to AGF_{str} follow the same trend as the analytical formula, where a large R_{th}/u results in relatively low AGF_{str} losses and a small R_{th}/u in relatively large AGF_{str} losses. The discrepancy between the analytical formula and the numerical data is discussed in section 4.1. The high temperature scenarios (T_{inj} = 90 ˚C) show the same values for AGF_{str} losses at high R_{th}/u, indicating that regardless of density-driven flow, ambient groundwater flow losses for systems with high R_{th}/u-values are minimal, indicating that other processes than *AGF* dominate losses. Going towards a smaller R_{th}/u, high temperature scenarios start to show more scatter compared to the low temperature scenarios, but with a similar trend. The scatter shows that some high temperature scenarios show higher AGF_{str} losses relative to the low temperature scenarios and some show lower AGF_{str} losses. To analyse which scenarios result in this discrepancy between the high and low temperature storage systems, the T_{inj} = 30 ˚C and T_{inj} = 90 ˚C are compared with each other in terms of AGF_{str} losses *(Figure 17*).

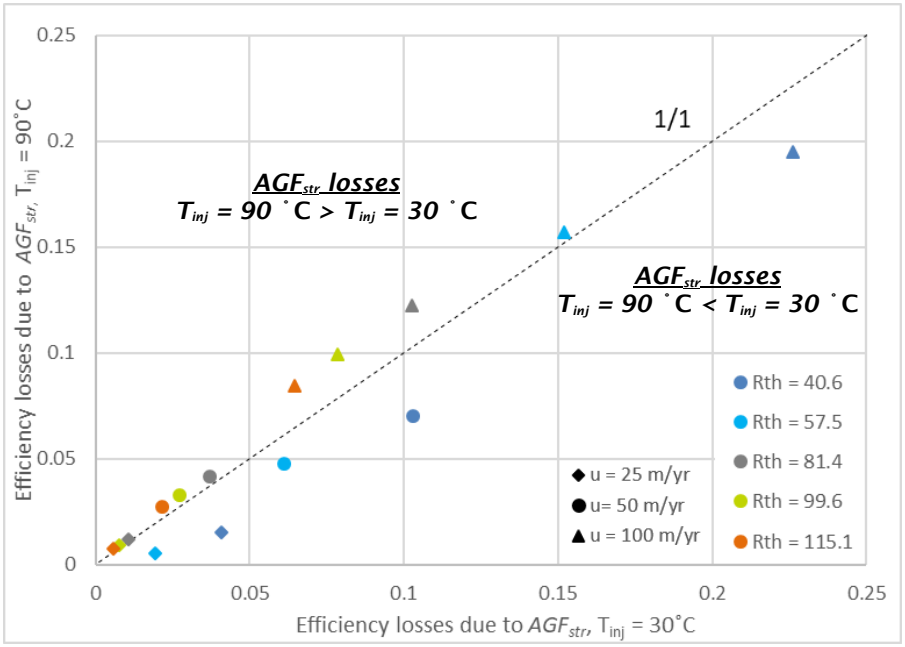

Figure 17 Comparing efficiency losses due to AGF_{str} between scenarios with T_{inj} = 30 ˚C and T_{inj} = 90 ˚C. Storage sizes are indicated with their corresponding maximum thermal radius (color). The ambient groundwater flow velocity corresponding to a scenario is given by the shape of the marker.

Generally, the graph shows that the relatively small high temperature systems experience less losses due to AGF_{str}, whereas large high temperature systems experience more losses due to AGF_{str} compared to the low temperature scenarios. For the larger systems, the relative difference in efficiency losses due to AGF_{str} depends on the velocity, where an increase in AGF_{str} velocity increases the relative increase in losses. For the smallest system, the amount of velocity does not play a significant role. The scenarios with a maximum thermal radius of 58 m shows that the increase in velocity results in a transition of lower efficiency losses (*u=25 m/yr, u=50 m/yr*) towards higher efficiency losses (*u=100 m/yr*) due to AGF_{str}. Considering the result that larger systems have relatively less efficiency losses due to density driven flow, the results with AGF_{str} indicate that for high temperature systems, AGF_{str} has more effect on the system when density-driven flow is minimal. Moreover, the effect of AGF_{str} on the system decreases when either the significance of density-driven flow or AGF_{str} velocity increases. To clarify these implications, the high temperature scenarios (T_{inj} = 90 ˚C) with V_{str} = 800.000 m^3/yr and V_{str} = 100.000 m^3/yr, both with ambient groundwater velocities of 100 m/yr, are analyzed in the following section since these scenarios show both ends of the spectrum with respect to AGF_{str} losses compared to low temperature scenarios.

3.3.2 Thermal geometry of HT-ATES systems with ambient groundwater flow in the storage aquifer

3.3.2a viscosity effect on tilting of the thermal front

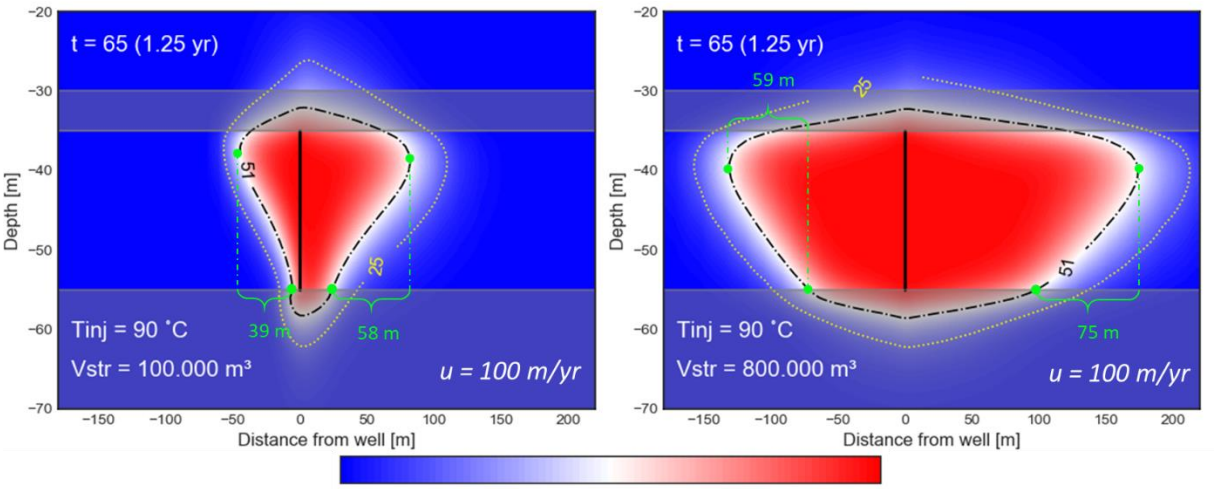

Figure 18 Vertical thermal cross-sections through the well in direction of ambient groundwater flow present in the sotrage aquifer. The injection temperature is 90 and a storage storage volumes are 100.000 m³/yr (left) and 800.000 m³/yr (right). The cross sections are taken at the end of the first full injection period (t = 65, 1.25 yr). The distance over which tilting takes place is highlighted in green and the 51 °C and 25 °C temperature contours are highlighted with a black and yellow line.

Overall, the addition of ambient groundwater flow in the storage aquifer results in a displacement of the injected thermal volume in direction of flow. The cross-sections in *Figure 18* show that the thermal shape changes, where at the upgradient (left area in cross-section), the distance over which tilting takes place decreased and in the downgradient, the distance over which tilting takes place increased compared to the scenarios with no AGF_{str}. Thus, the distance over which tilting takes place is affected by the ambient groundwater flow. Considering the explanation about the effect of viscosity on thermal front tilting in section 3.2.2b, the decrease in horizontal flow at the upgradient results in a decrease in tilt, and the increase in horizontal flow at the downgradient results in an increase in tilt.

3.3.2b Evolution of the thermal geometry over time

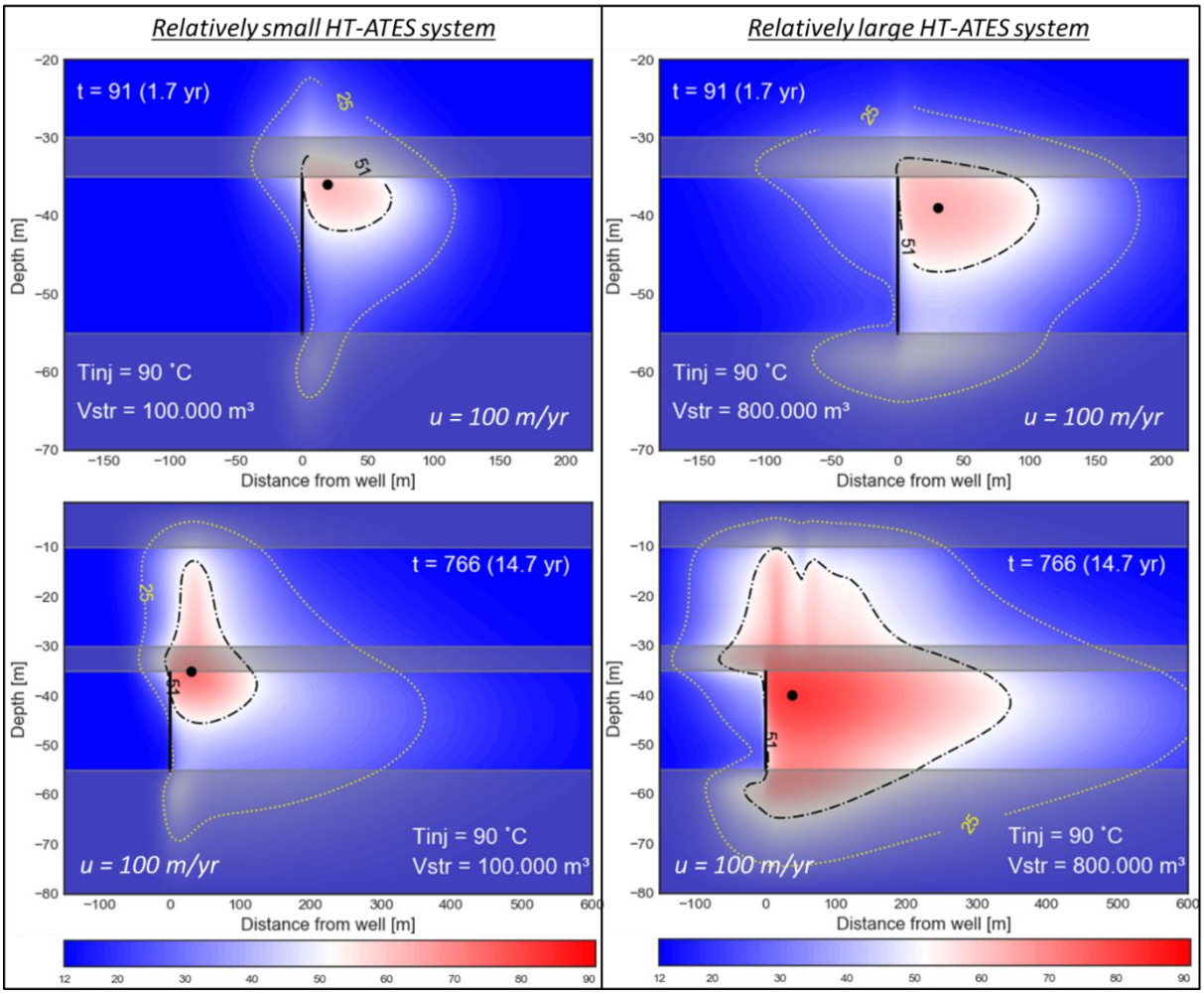

Figure 19 Vertical thermal cross-sections through the well in direction of ambient groundwater flow present in the sotrage aquifer. The injection temperature is 90 and a storage storage volumes are 100.000 m³/yr (left) and 800.000 m³/yr (right).The thermal cross-sections are taken at the end of extraction after the first full operational cycle (t = 91, 1.7yr) (top) and the last full operational cycle (t = 766, 14.7 yr) (bottom). The contour lines of 25°C and 51°C are highlighted.

The thermal cross-sections made at the end of extraction give an idea of how the residual heat evolves through the subsurface over time (*Figure 19*). Generally, the heat is displaced in direction of flow, resulting in much residual heat to be present in the downgradient direction of the well. At the upgradient, little residual heat is present. Additionally, density-driven flow still moves a considerable amount of heat upwards in the storage aquifer, indicating that the presence of density driven flow is still significant. Comparing the cross-sections at the end of extraction after the first operational year (*Figure 19 top*), the larger system leaves absolute more energy behind, resulting in overall more residual heat in the subsurface after 15 years (*Figure 19 bot*). Comparing the thermal cross-sections made at the end of the last years full operational cycle (*Figure 19 bot*) shows a significant difference in thermal spreading between the small and large system. In the small system, residual heat is mainly accumulating at the top of the storage aquifer. For the large system, residual heat is present over the entire depth of the storage aquifer.

For both scenarios, the thermal geometry in the overlying aquifer changes when flow is present in the storage aquifer. For the small system, AGF_{str} moves the primary peak of heat, which arises from the well, in direction of flow (*Figure 19 bot. right*). For the large system, the right part of the secondary circle detaches in direction of flow and becomes a new peak (*Figure 19 bot. left*). The detached heat peak is a result of the residual heat at the top of the storage aquifer due to density-driven flow that is not extracted. The secondary heat circle at the left side of the thermal cross-section is not present because of all heat at the left side of the storage aquifer being consumed during extraction. The cross-sections give an overview of how the development of heat is in the subsurface. Based on the difference in the thermal cross-sections, two theoretical interpretations are constructed that provide an explanation for the difference in relative AGF_{str} losses. These are explained and discussed in section 4.3.

3.3.2c Horizontal spreading of the thermal volume

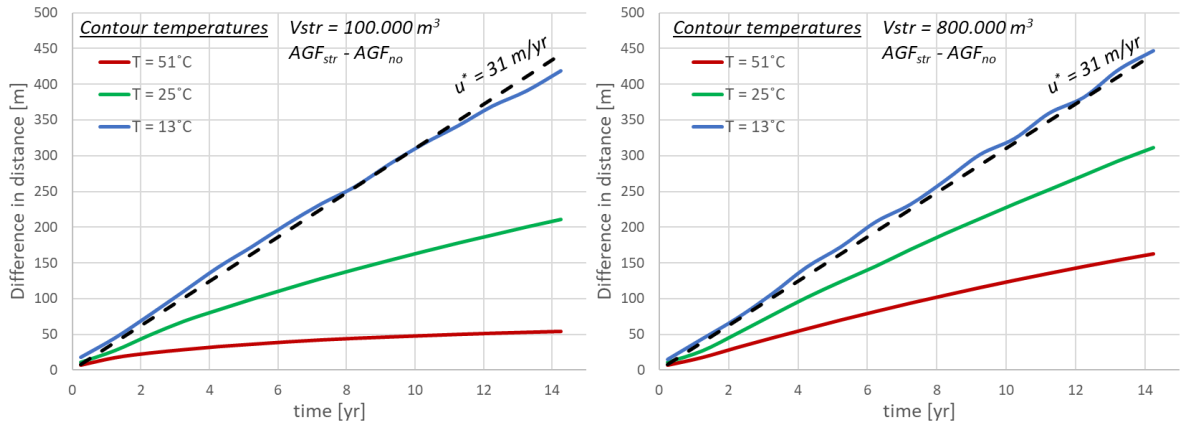

Figure 20 The distance travelled of 13˚C, 25˚C and 51˚C water over time for a system with ambient groundwater flow in the storage aquifer. The distance travelled is measured at the top of the storage aquifer. The system with an injection volume of 100.000 m³ (left) and 800.000 m³ (right) are displayed. The dotted line is the distance over time for AGF corrected with the retardation factor of the heat.

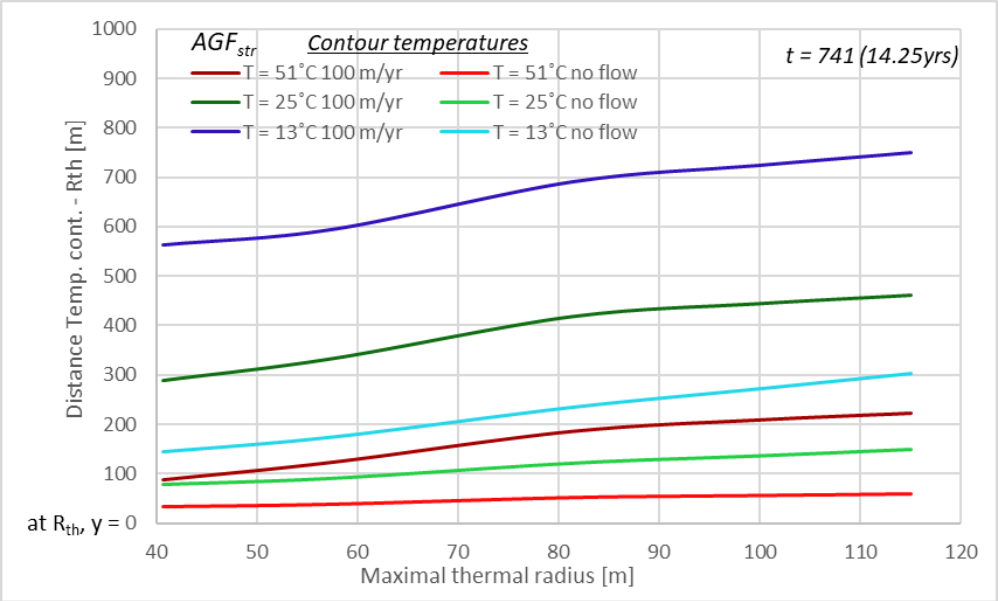

Figure 21 Distance travelled of heat over the maximum thermal radius for systems with and without 100 m/yr of ambient groundwater flow in the storage aquifer. The Distances are measured from the corresponding thermal radius onwards.

To analyze horizontal spreading, the difference in distance travelled by the 13˚C, 25˚C and 51˚C water in downgradient direction, between AGF_{str} *(v = 100 m/yr*) and AGF_{no} scenarios with storage sizes of V_{str} = 100.000 m^3 and 800.000 m^3 are presented (*Figure 20*). The distance travelled is measured at the top of the storage aquifer at the end of every injection period to clear the oscillation pattern, facilitating the analysis. Additionally, the distance travelled of the heat at the end of the last injection cycle (*t = 741, 14.25 yr*) is plotted over the maximum thermal radius of a system.

Comparing the increase in temperature contour distances from the initial (AGF_{no}) of both systems, heat travels less far horizontally in direction of *AGF* and reaches a constant distance from the initial distance for the smaller system (V_{str} *= 100.000 m³*). The larger system shows an increase in spreading from the initial of approximately 300 meters for the 25 ˚C, whereas for the smaller system its ±200 meters. Furthermore, the 51 ˚C is at a constant distance of 50 meters from the initial location, whereas for the larger system, the difference in distance is still increasing. For the 13 ˚C, regardless of storage size, the contour travels generally at the same speed away from the initial location as the velocity of ambient groundwater flow corrected with the retardation factor (u^* *= 31 m/yr*). Overall, temperature distances indicate that ambient groundwater flow will spread heat

further, over a longer period of time, for systems with a relatively larger storage volume. *Figure 21* supports this since it shows an increase in spreading for a larger system. The small nod in the graph is because of the smaller systems going towards steady state earlier.

The increase in spreading due to ambient groundwater flow for a larger system is due to a larger system displacing more absolute energy outside of the well catchment. Additionally, this gives an explanation why the larger system takes longer for it to reach steady state. Steady state is attained when eventually the heat that is not extracted by the well (residual heat) and the heat loss due to cooling by the ambient groundwater reach an equilibrium. Increasing the systems storage volume results in absolute more energy in the system which is displaced out of the well catchment by ambient groundwater flow. Since the cooling effect of the ambient groundwater stays relatively the same, the larger amount of heat outside of the catchment area needs a longer time to develop into a steady state with the cooling of the ambient groundwater. Since more energy falls out of the catchment, high temperatures spread further and steady state takes longer to reach. Overall, the increase in horizontal spreading due to ambient groundwater flow when increasing the storage size should be considered when realizing a larger HT-ATES system.

3.4 HT-ATES systems with ambient groundwater flow in the overlying aquifer

The impact of flow in the overlying aquifer depends on the thickness of the middle aquitard that separates both aquifers. Results of changing the aquitard thickness are presented first in order to provide an understanding of its impact on the system. Subsequently, the results of flow in the overlying aquifer are discussed in the same structure as the previous presented results.

3.4.1 Thickness of the middle aquitard

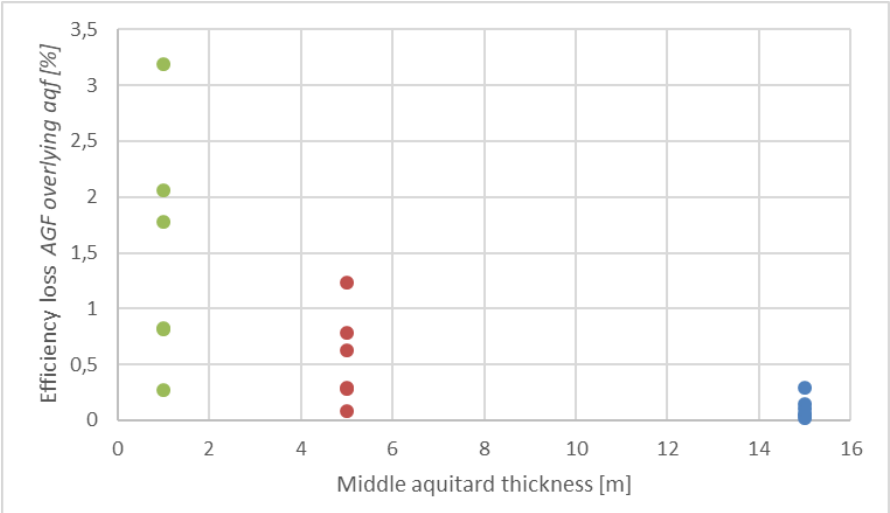

Figure 22 Efficiency loss due to flow in the overlying aquifer over thickness of the middle aquitard thickness.

Scenarios modelled with an alternating middle aquitard thickness are compared in terms of recovery efficiency (*Figure 22*) and well temperature distribution in the storage aquifer (*Figure 23*). Appendix 1 gives an overview of the scenarios modelled and the values for the last year recovery efficiencies. Scenarios with a middle aquitard of 1 meter show the highest losses in efficiency compared to scenarios with a thicker middle aquitard, indicating that a thinner middle aquitard results in overall higher efficiency losses. Furthermore, the difference in efficiency losses is the largest for scenarios with a middle aquitard of 1 meter, where the highest loss is 3.2% and the lowest 0.25%. Having a middle aquitard thickness of 15 meters results in efficiency losses to be between 0 - 0.3% indicating that the variation in recovery efficiency increases when a thinner middle aquitard is present. The well temperatures show that early in operation (*t = 142, 2.7 yr*), well temperatures in the top part of the storage aquifer are lower for scenarios with a thinner middle aquitard (*Figure 23 left*). Over time, the temperatures through the whole well in the storage aquifer decrease ±3 °C (*Figure 23 right*).

Other than the middle aquitard thickness, the properties of the middle aquitard, such as hydraulic and thermal conductivity, influence the amount of heat lost at the top of the storage aquifer. The low hydraulic and thermal conductivity result in no flow and low conduction rates from the heat in the storage aquifer towards the overlying aquifer. Once the heat arrives in the overlying aquifer, it experiences density-driven flow and more conduction due to the relatively higher hydraulic and thermal conductivities. Because of the presence of density-driven flow and the increase in conductivity, the heat is able to spread, enabling more heat to accumulate in the overlying aquifer. Changing the thickness of the intermediate aquitard changes the distance that the heat has to travel through a low thermal conductive area, affecting the pace in which the heat enters the overlying aquifer. Therefore, when having a thin middle aquitard, heat spreading towards the overlying aquifer starts relatively early and enters relatively fast, resulting in overall more losses in recovery efficiency. Ambient groundwater flow in the overlying aquifer is expected to result in more vertical conduction rates from the storage aquifer to the overlying aquifer because of the increase in the spreading of heat in the overlying aquifer.

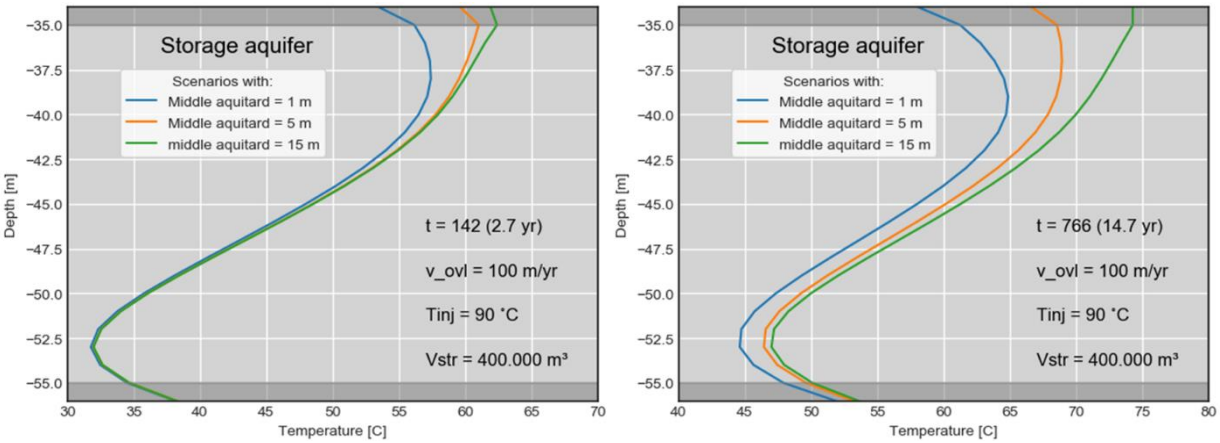

Figure 23 Temperature profiles through the well in the storage aquifer for scenarios with V_{str} = 400.000 m³, T_{inj} = 90 °C and v_{ovl} = 100 m/yr. The profiles are taken at the end of extraction, after the second full operational cycle (left) and after the last full operational cycle (right).

3.4.2 Analysis of HT-ATES systems performance with *AGF* in the overlying aquifer

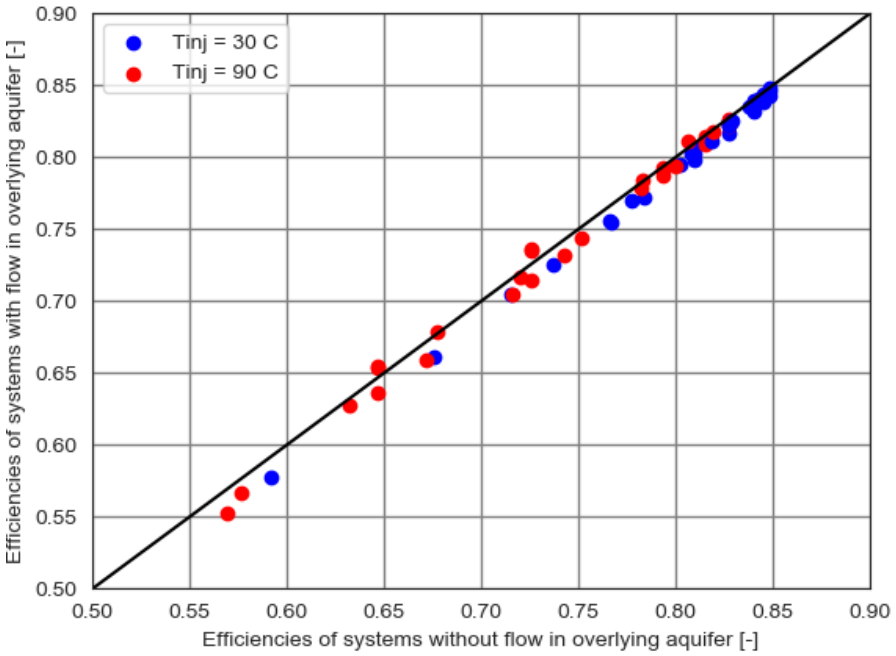

Figure 24 Comparing efficiencies of systems with and without AGF in the overlying aquifer. A distinction is made between scenarios with T_{inj} = 30˚C and T_{inj} = 90˚C

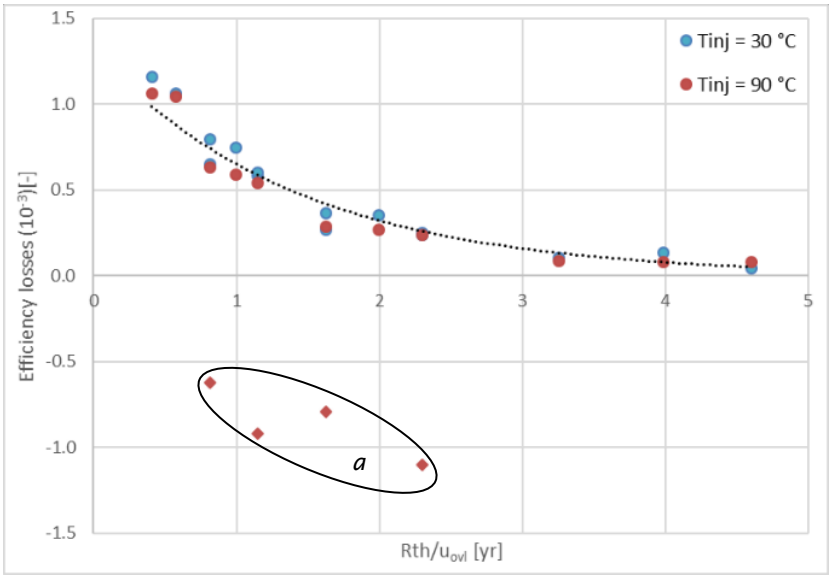

Figure 25 Efficiency losses due to flow in the overlying aquifer relative to R/u_{ovl}. Four scenarios show an increase in efficiency (a).

Comparing scenarios with flow in the overlying aquifer (AGF_{ovl}, AGF_{bth}) with scenarios that have no flow in the overlying aquifer (AGF_{no}, AGF_{str}) shows that the addition of flow causes minor losses in recovery efficiency (0.5-1%) (*Figure 24*). No significant difference in losses are observed when utilizing a higher injection temperature. Considering that conduction towards the overlying aquifer is a small percentage of the losses and that AGF_{ovl} causes a minor change in conduction, efficiency losses of 0.5-1% are seen as acceptable outcomes. *Figure 25* shows that when plotting the efficiency losses over R_{th}/u_{ovl}, a similar trend as the efficiency losses of *AGF* in the storage aquifer when plotting over R/u_{str} (*Figure 16*) is present. Considering that the AGF_{ovl} velocity and the size of the storage aquifer impact the relative losses in vertical conduction losses, a similar relation for efficiency over R/u_{ovl} is possible. Furthermore, four scenarios show an increase in efficiency compared to AGF_{no} scenarios (indicated with *a* in *Figure 25*). To elaborate on these four results, one of the thermal cross-sections in the next section is from a scenario that shows an increase in efficiency.

3.4.3 Thermal geometry of HT-ATES systems with ambient groundwater flow in the overlying aquifer

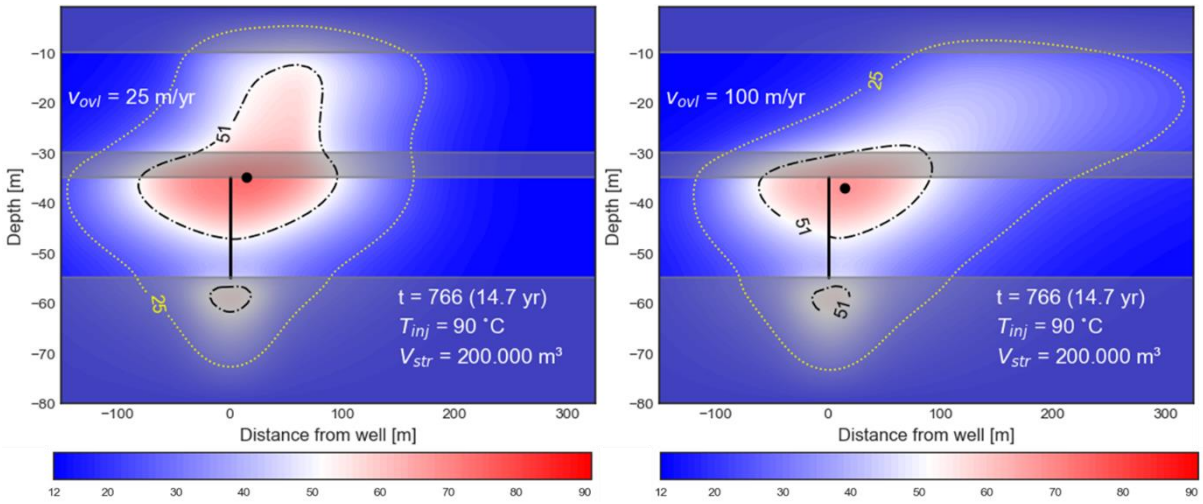

Figure 26 Thermal cross-sections in direction of ambient groundwater flow of scenarios with a storage volume of 200.000 m³, taken at the end of extraction of the last full operational cycle. The scenarios have flow in the overlying aquifer of 25 m/yr (left), and 100 m/yr (right). The black dot in the cross-section represents the center of heat.

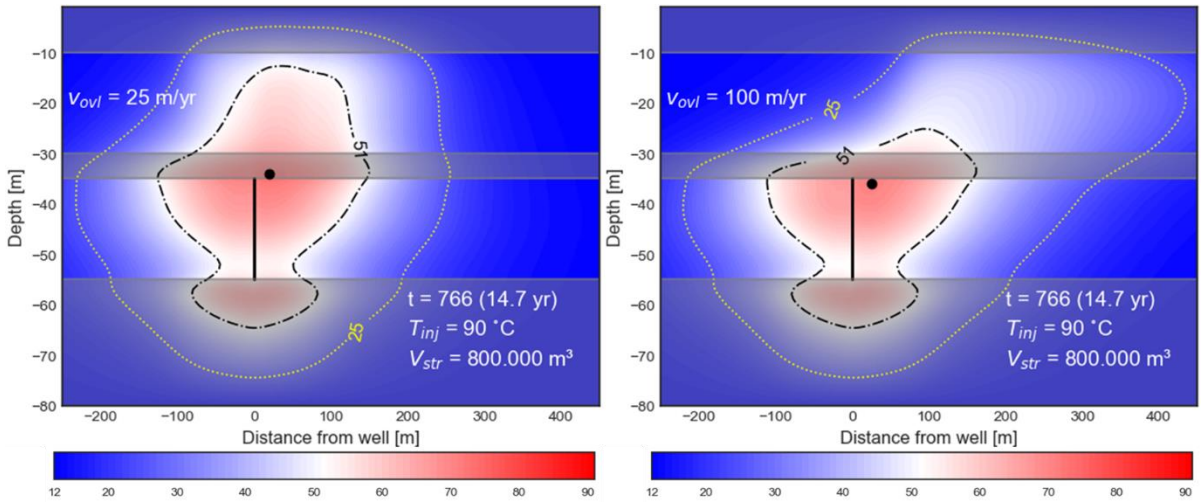

Figure 27 Thermal cross-sections in direction of ambient groundwater flow of scenarios with a storage volume of 800.000 m³, taken at the end of extraction of the last full operational cycle. The scenarios have flow in the overlying aquifer of 25 m/yr (left), and 100 m/yr (right). The black dot in the cross-section represents the center of heat.

The thermal cross sections of scenarios with ambient groundwater flow in the overlying aquifer generally show that the impact of thermal spreading increases horizontally and decreases vertically in the overlying aquifer (*Figure 26 &Figure* 27). The horizontal spreading increases in the overlying aquifer when the AGF_{ovl} velocity increases (*Figure 26 &*Figure 27). Additionally, the overall temperatures in the overlying aquifer are reduced when flow is present, where the 51 *°C* contour moves downwards when the AGF_{ovl} velocity increases. In the storage aquifer, other than the displacement of the center of heat in direction of AGF_{ovl}, the thermal geometry stays relatively the same for scenarios with efficiency losses. For the smaller system with a AGF_{ovl} *velocity of 25 m/yr*, a difference in residual heat in the storage aquifer is observed, where the scenario with a lower velocity has more residual heat and overall higher temperatures in the storage aquifer compared to the scenario with a high AGF_{ovl} velocity (v_{ovl} *= 100 m/yr*).

Since the two V_{str} = *200.000 m³* scenarios also differ in giving a positive and a negative result on the recovery efficiency relative to the no *AGF* scenario, further analysis of the results in provided by looking at the energy balances of the different layers in the systems. The energy balances are at the end of extraction of the last full operational cycle (t = 766, 14.7 yr). The Total Energy [*J*] shows that adding flow in the overlying aquifer results in more energy to remain in the system in both AGF_{ovl} cases. However, the distribution of the energy between the layers differs.

For the u_{ovl} = *100 m/yr* scenario, every layer apart from the top aquitard shows an increase in residual energy compared to the u_{ovl} = *0 m/yr* scenario. The increase in energy in the overlying aquifer means that more energy is lost vertically upwards. The increase in energy losses in the storage aquifer and the surrounding aquitards is due to the displacement of heat in the overlying aquifer. Relating the efficiency losses towards the thermal cross-sections and the energy distribution between the layers, the increase in losses is related to the increase in vertical conduction and a minor displacement of heat horizontally. For the v_{ovl} = *25 m/yr* scenario, residual heat in the middle aquitard and storage aquifer is higher, whereas in the overlying aquifer and the other aquitards, residual energy is lower. The lower energy levels in the overlying aquifer indicate that less energy is vertically conducted towards the overlying aquifer. Viscosity differences between the cold water in the overlying aquifer and the hot water in the middle aquitard provide an explanation for this result, where density-driven flow is diminished due to the less viscous cold water above the hot water which acts as a hypothetical barrier for vertical upward flow. This result shows the impact of a viscosity difference on systems with flow in an overlying aquifer and is further discussed in section 4.2.

V_{str} = 200.000 m³, T_{inj} = 90 °C	u_{ovl} = 0 m/yr	u_{ovl} = 25 m/yr	u_{ovl} = 100 m/yr
Top aquitard	8,26E+12	7,28E+12	6,84E+12
overlying aquifer	5,07E+13	4,77E+13	5,23E+13
middle aquitard	2,04E+13	2,25E+13	2,24E+13
storage aquifer	6,34E+13	7,02E+13	6,83E+13
bottom aquitard	2,43E+13	2,06E+13	2,54E+13
Total Energy [J]	1,67E+14	1,68E+14	1,75E+14

Table 3 The amount of residual energy after last year of extraction (t = 766, 14.7 yr) for systems with a storage size of 200.000 m³ and flow in the overlying aquifer.

3.5 HT-ATES systems with ambient groundwater flow in both aquifers, same direction

3.5.1 Analysis of HT-ATES systems performance with *AGF* in both aquifers

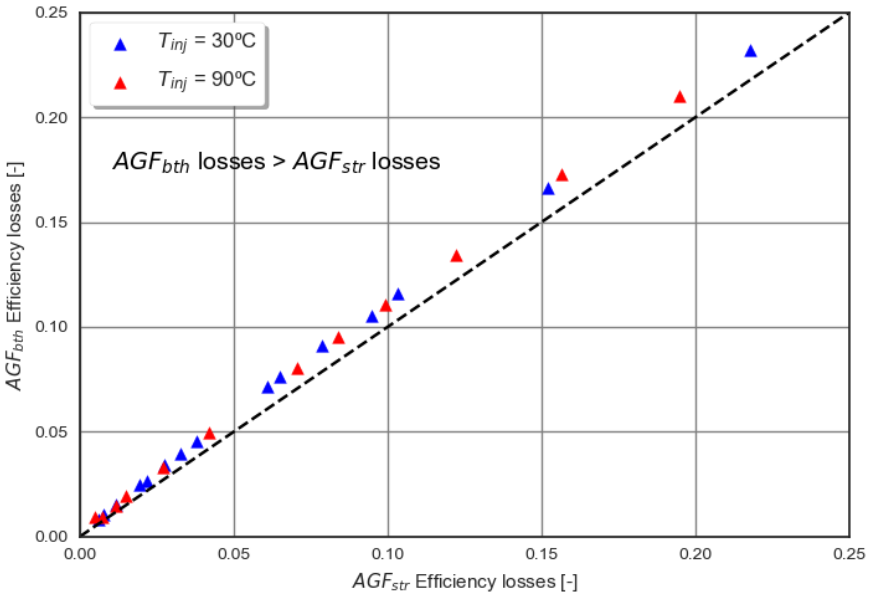

Figure 28 Comparing efficiencies losses of systems with AGF in the storage aquifer and AGF in both aquifers for T_{inj} = 30˚C and T_{inj} = 90˚C scenarios.

The AGF_{bth} efficiency losses are compared with the AGF_{str} efficiency losses (*Figure 28*) which shows that having flow in both aquifers results in a slight increase (0.1-2 %) in efficiency losses due AGF_{bth}. Overall, the increase in loss is relatively low. Systems with relatively high *AGF* losses experience more loss when flow in both aquifers occur. To understand where the losses occur relative to when there is no flow or *AGF* in the storage aquifer, the energy balance per layer for the AGF_{no}, AGF_{str} and AGF_{bth} base scenarios (V_{str} = 400.000 m^3, T_{inj} 90 ˚C) are presented (Table 4). The total residual energy increases significantly when flow in the system is present. Having flow in both aquifers results in an increase in residual energy in every layer except for the top aquifer. For the AGF_{str} scenario, residual energy in every layer increases. Comparing the AGF_{str} and AGF_{bth} shows that every layer, except the top aquifer, has an increase in residual energy, indicating that the increase in loss is over the whole subsurface. In section 4.2c a possible explanation for the losses is given.

V_{str} = 400.000 m^3, T_{inj} = 90 ˚C	***No flow* u = 0 m/yr**	***Flow storage* u_{str} = 100 m/yr**	***Flow both* u_{bth} = 100 m/yr**
Top aquitard	1.10E+13	1.21E+13	1.10E+13
overlying aquifer	7.40E+13	8.98E+13	9.27E+13
middle aquitard	3.50E+13	4.56E+13	4.83E+13
storage aquifer	1.17E+14	1.71E+14	1.77E+14
bottom aquitard	4.34E+13	5.75E+13	5.81E+13
Total Energy [J]	2.80E+14	3.76E+14	3.88E+14

Table 4 The amount of residual energy per layer for the AGF_{no}, AGF_{str} and AGF_{bth} base scenarios (V_{str} = 400.000 m^3, T_{inj} 90 ˚C) at the end of extraction of last years full operational cycle (t = 766, 14.7 yr)

4. Discussion

4.1 The linear approximation for density change over temperature

In the model, a linear approximation is used for the change in density over increasing temperature, mainly affecting flow in vertical direction. The approximation causes an overestimation of high-temperature densities and an underestimation of low-temperature densities. As a result, low temperature water experiences more buoyancy flow whereas high temperature water less. Within the storage aquifer, the approximation is expected to cause minor errors since flow is generally horizontal by *AGF* and/or well operation. Additionally, the linear approximation translates into buoyancy flow that counters each other when tilting of the thermal boundary takes place. At the bottom of the thermal radius, more density flow experienced by cold water will be compensated with less density flow from the hot water. However, residual heat, mainly consisting of low temperature water, will experience more density-driven flow than realistic, resulting in more heat at the top of the aquifer and therefore more conduction towards the overlaying aquifer. Additionally, this will have its effects on well operation in later years. Injected water will flow easier in the top part of the storage aquifer because of the residual heat, causing the region to be more vicious than the bottom of the storage aquifer. Therefore, flow in the top of the storage aquifer will be enhanced compared to flow in the bottom part, resulting in more tilting of the thermal front.

The approximation is expected to cause larger errors in vertical thermal spreading for the overlying aquifer. Relatively low temperatures will enter the overlying aquifer through conduction that experience unrealistic high amounts of density-driven flow, resulting in an overestimation of vertical flow. When AGF_{ovl} is added, density-driven flow is expected to slightly diminish because of the viscosity difference between the cold ambient groundwater and the conducted hot water, resulting density-driven flow to be less dominant and results to be closer to reality. However, for scenarios without AGF_{ovl}, temperature contours in the overlying aquifer are vertically amplified due to the overestimation.

4.2 The influence of an overlying aquifer

4.2a Density driven flow

The results show that HT-ATES systems cause for a significant increase in heat in the overlying aquifer compared to LT-ATES. Other than the tilting of the thermal front, high conduction losses towards the overlying aquifer are considered to be part of the increase in losses due to density-driven flow. This can be explained by imagining what the combination of density-driven flow in both aquifers would result in. Density-driven flow in the storage aquifer results in a constant supply of heat towards the upper part of the storage aquifer. Density-driven flow in the overlying aquifer removes heat at the bottom of the overlying aquifer which is replaced with cold ambient groundwater. If the heat in the overlying aquifer has enough space to move to, the temperature gradient between the two aquifers stays relatively high, resulting in more conduction losses.

4.2b Ambient groundwater in one of the two aquifers

The conduction towards the overlying aquifer changes when $AGF_{ovl\ is}$ added. The results show that thermal spreading in vertical direction decreases and in horizontal direction increase. Overall, the scenarios suggest that the increase in spreading towards the overlying aquifer are a result of an increase in dispersion and the horizontal displacement of the conducted heat, resulting in a larger temperature gradient and more conduction losses towards the overlying aquifer. For most of the scenarios, this is seen as the dominant processes causing the loss in efficiency. However, the scenarios that cause an increase in efficiency expose another possible interaction between processes.

The results of energy per layer (Table 3 The amount of residual energy after last year of extraction (t = 766, 14.7 yr) for systems with a storage size of 200.000 m^3 and flow in the overlying aquifer.) show that less energy is conducted towards the overlying aquifer which is related to the a decrease in density driven flow. The effect of density-driven result is diminished due to the difference in viscosity between the conducted hot water and the ambient groundwater. The more viscous ambient groundwater flows over the conducted hot water, causing it to move horizontally but also less vertically. If the displacement in horizontal direction is rather small, the decrease in vertical flow causes a decrease in conduction losses through the middle aquitard. Generally, the

decrease in density-driven flow due to ambient groundwater flow in the overlying aquifer is present in every scenario, only in the scenarios with high AGF_{ovl} velocities, the horizontal displacement is dominant.

4.2c Ambient groundwater in both aquifers

Having flow in both aquifers generally results in a decrease in efficiency compared to the scenarios with flow only in the storage aquifer. Assessing the results, two theories are constructed that cause the increase in efficiency losses: (1) Conduction towards the overlying aquifer increases when flow in both aquifers is present because of overall larger temperature gradient between the injected volume and the overlying aquifer. (2) The displacement of heat in both aquifers causes the conducted heat towards the overlying aquifer to move with the residual heat in the storage aquifer. Therefore, higher temperatures are present at the top boundary of the injected heat in the storage aquifer, leading to lower vertical conduction rates. Heat that normally would be lost due to conduction now stays in the storage aquifer but is lost due to AGF_{str}. According to the energy per layer balance (Table 4), except for the top aquitard, show an increase in residual energy is seen when comparing the scenarios with flow in both to the scenarios with flow in the storage aquifer. Therefore, both of the theories are assumed to occur. Which process is dominant where cannot be stated with the results. However, the results do show that having an overall larger horizontal displacement results in higher losses and should be taken in consideration.

4.3 Ambient groundwater flow in the storage aquifer

4.3a Relative difference in AGF_{str} losses between HT-ATES and LT-ATES

Before the theoretical interpretation about the relative difference in AGF_{str} losses between HT-ATES and LT-ATES can be explained, the impact of ambient groundwater flow on conduction and dispersion has to be understood. In terms of dispersion, the increase in horizontal flow rate may increase the dispersion. However, in our scenarios, the maximum *AGF* velocity causes a relatively low increase in the dispersion coefficient and is therefore considered negligible. In terms of conduction, ambient groundwater flow results in an increase in spreading of heat over a larger horizontal area and therefore more conduction losses. For our scenarios, where the systems are relatively flat, the increase in horizontal area over which conduction takes place to the overlying aquifer is particularly of interest because of the presence of an overlying aquifer and the accumulation of heat in this area due to density-driven flow.

Considering the explanation for more conduction losses for HT-ATES as described in section 3.2.1, it is assumed that when the area over which conduction takes place increases due to AGF_{str}, relatively more conduction losses are expected for HT-ATES compared to LT-ATES because of the relative higher conduction losses.

AGF_{str} losses relatively lower for HT-ATES compared to LT-ATES

The losses due to a change in dispersion and conduction are assumed to effect the efficiency of relatively small HT-ATES systems. However, the relatively lower AGF_{str} losses compared to LT-ATES are presumed to be due to the density-driven flow dominating the losses. By observing the thermal cross sections of small systems either with AGF_{str} or without, a theoretical interpretation for the relatively lower losses is given. The change in thermal front tilting is considered to have a minor impact.

Imagining a small HT-ATES system of which the storage volume is fully injected (*Figure 18* left). Ambient groundwater flow moves the entire injected volume in direction of the flow. At the bottom of the storage aquifer, heat is moved, however, ambient groundwater flow does not impact the extraction of the heat because of the thermal volume still being within the catchment of the well after displacement. Therefore, the efficiency is not effected due to ambient groundwater flow in the lower part of the storage aquifer. In the upper part of the storage aquifer, a relatively larger thermal radius is present because of the tilting of the thermal front, leading to a larger R_{th}/u. The thermal volume is effected but relatively less and therefore resulting in less loss. This overall reduction in the effect of ambient groundwater flow on the total storage aquifer is considered to cause the decrease in AGF_{str} losses.

AGF_{str} losses relatively higher for HT-ATES compared to LT-ATES

Large HT-ATES systems that have a R_{th}/u lower than 2 show a relatively higher loss due to AGF_{str} which increases when the velocity of AGF_{str} is increased. Thermal cross-sections of these scenarios reveal that temperatures

higher than the average temperature in the system (T = 51) reach until the bottom of the aquifer. Therefore, it is assumed that AGF_{str} displaces heat over the whole storage aquifer out of the catchment of the well. Considering the explanation for an increase in losses due to more conduction towards the overlying aquifer, the relatively higher losses due to AGF_{str} for HT-ATES compared to LT-ATES are considered to be because of more vertical conduction losses towards the overlying aquifer while horizontal losses are relatively similar.

Assessment of the theoretical interpretation

The theoretical interpretation for the difference in AGF_{str} losses has been assessed by looking at the total energy for each layer at the end of extraction of the last full operation cycle (t = 766, 14.7 yr). These are calculated as explained in section 2.1.2. However, assessment by looking at the energies is found to be inconvenient because of several reasons. First, the energy injected in the system for HT-ATES and LT-ATES is significantly different, complicating the comparison of both. Secondly, the amount of injected energy between storage sizes and the initial distribution in scenarios where no ambient groundwater flow is present differs significantly. When calculating the relative change in energy per layer due to ambient groundwater flow, each storage size has a different initial energy distribution. Therefore, comparing different storage sizes results in inaccurate interpretations. Thus, to validate this theoretical interpretation, it is proposed to simplify the model by modelling only the storage aquifer. By doing so, conduction towards the aquitard above the storage aquifer would be more consistent, facilitating the interpretation of energy levels in the system.

4.3b The analytical formula

In this study, the numerically calculated efficiency losses due to *AGF* in the storage aquifer were found to be generally lower than those calculated with the analytical formula of Bloemendal & Hartog 2018. The discrepancy may lie in the difference in approach, where the analytical formula is a simplified representation of the effects of ambient groundwater flow. The numerical data is more complex because of the change in discharge of the well for each time step and the addition of conduction/dispersion and density-driven flow.

In terms of pumping operation, the analytical formula assumes one size for the thermal radius. The numerical data has a change in thermal radius for each timestep because of the sinusoidal pumping regime. Therefore, the catchment of the well changes at each time step during extraction. Additionally, the change in conduction and dispersion losses are included in the AGF_{str} losses when looking at the relative change in efficiency between scenarios with and without AGF_{str}. Changes in these conduction losses are embedded in the AGF_{str} losses as proven with the AGF_{bth} scenarios. Altogether, the discrepancy between the numerical data and the analytical formula can be therefore related to the simplification of the analytical formula compared to the complex numerically modelled scenarios.

However, the analytical formula does provide a simple, fast and effective method of evaluating whether ambient groundwater flow in a certain area would have major impact on the efficiency of an HT-ATES or LT-ATES system. For HT-ATES, ambient groundwater flow losses might be slightly higher when density-driven losses are brought to a minimum due to more conduction losses. Nonetheless, realizing a system of which the R_{th}/u value would be lower than 2.5 results in significant losses due to ambient groundwater flow and should therefore be avoided. When the R/u value is higher than 3, other processes than ambient groundwater flow are dominant in producing the losses.

4.4 Model limitations

4.4.1 Horizontal discretization

It should be noted that the discretization of the model shows an unrealistic distribution of the residual heat in diagonal direction. Because of the usage of the finite-difference method, grid-cells are scaled logarithmically in x and y direction. Cells in diagonal direction are therefore scaled in x and y direction simultaneously, resulting in a courser discretization than in x and y direction of the well. For scenarios without *AGF,* the bubble in the storage aquifer at the end of injection does not seem to be influenced by this. However, the residual heat at the end of extraction in both aquifers does show less accumulation of heat in the diagonal direction while the heat distribution should be axis-symmetric (*Figure 29 left*). When adding *AGF*, a gap in residual heat in diagonal direction of the well is observed in the overlying aquifer (*Figure 30 left*). The observations with no *AGF* give confidence that this geometry in scenarios with *AGF* is a result of a fault in discretization.

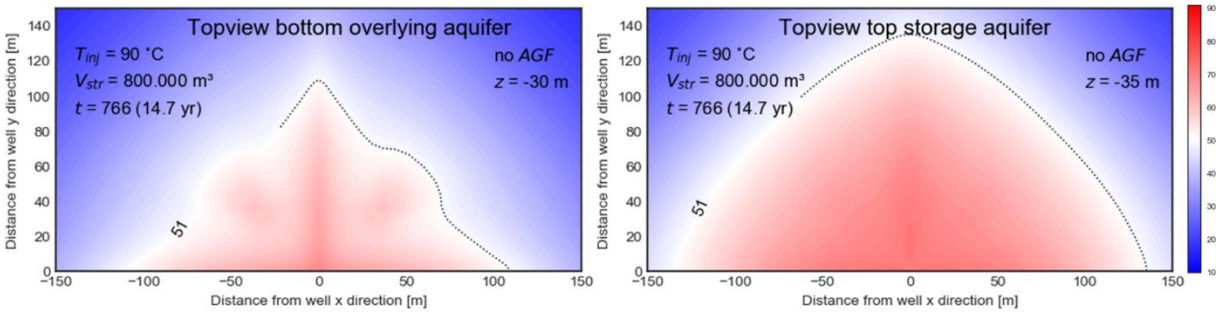

Figure 29 Topview thermal contour plot from a scenario without ambient groundwater flow, taken at the bottom of the overlying aquifer (left) and the top of the storage aquifer (right) to illustrate the influence of the discretization on the horizontal thermal distribution.

In the storage aquifer, the geometry is observed in the residual heat that is exposed and becomes less obvious in later operational years. The geometry is most clear when no *AGF* is present (*Figure 29*). With an increase in *AGF* velocity, the error in the geometry diminishes. During injection and extraction, the thermal volume shows no significant error due to the discretization. Therefore, it is assumed that the main effect of the discretization is that there is less heat that remains in the system, leading to more heat that is recovered and therefore higher recovery efficiencies. However, since the geometry does become less obvious in later years, it is believed that once the system is close to steady state, little of the error is still effecting the results in terms of spatial distribution and yearly recovery efficiency.

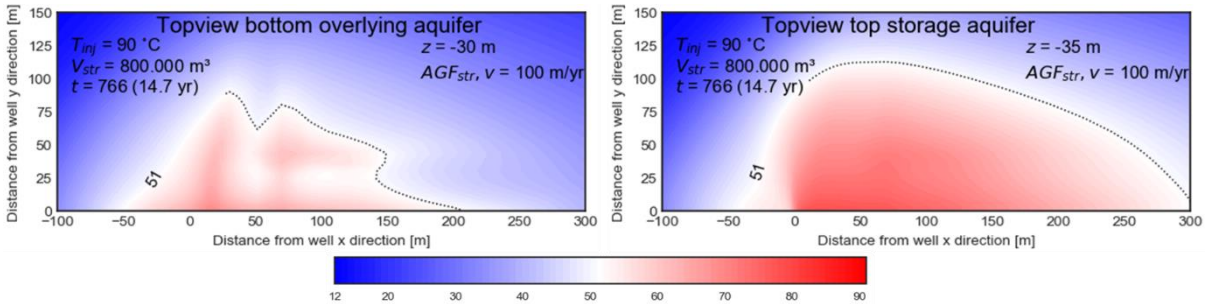

Figure 30 Topview thermal contour plot from a scenario with ambient groundwater flow in the storage aquifer, taken at the bottom of the overlying aquifer (left) and the top of the storage aquifer (right) to illustrate the influence of the discretization on the horizontal thermal distribution when AGF flow is present.

In the overlying aquifer, the change in geometry is more present because no diagonal flow interacts with courser cells. The geometry has influence on the conduction in upward direction. Since conduction towards the overlying aquifer and significant changes in these conduction patterns due to *AGF* show little effects on efficiency, it is presumed that the error does not alter the efficiencies significantly. In terms of geometry, the area in diagonal direction of the well does show lower temperatures that could contribute to the alteration of the thermal geometry (*Figure 30).* When no *AGF* is present, the geometry of the secondary peaks might show lower temperatures than reality. In scenarios with large volumes and high *AGF* velocities in the storage aquifer, the error can have a significant contribution to the separation of the secondary peak.

Overall, the error is assumed to cause no significant changes in efficiency, especially because the efficiencies used are those obtained over last year of operation and the error diminishes over time because of equal

distribution of residual heat over the system. The error does have the potential to have caused errors in the thermal geometry of the overlying aquifer. Therefore, the interpretation of the geometry in the overlying aquifer should be examined with care. However, cross-sections in x-direction are presumed to be valid because of the horizontal conduction rate being quite low.

4.6 Overestimated losses by model with 1 m thickness middle aquitard

The analysis of efficiency losses due to the alteration of the middle aquitard thickness shows generally good results. However, for the cases with an middle aquitard thickness of 1 meter, a higher influence of numerical dispersion could be expected. The cells in z-direction have the size of 1 meter, meaning that the middle aquitard consists of one cell in these scenarios. Because of the abrupt shift in geological layer, and therefore hydrogeological parameters, the finite-difference equations are likely to comprise errors in the computation, which are then numerically dispersed towards the overlying aquifer.

4.7 Measurements of the horizontal thermal spreading

It should be noted that the logarithmic scaling of the system could lead to discretization errors once far from the well. At a distance of 500 meters from the well, the cell sizes are approximately 60 meters, increasing towards 150 meters. Contour lines of the 25 and 13 $^{\circ}$C water at these distances could have errors since they travel much smaller distances than the size of the cells present. Therefore, the travelled distances presented of these contour lines should be seen as an approximate value, rather than the precise distance travelled.

4.8 The usage of multiple wells

This study provides an understanding of the physical processes that come with HT-ATES. However, in reality, a full HT-ATES system consists of at least two wells (a hot and a cold water well). When realizing HT-ATES, the interplay between both of such wells should be considered. Temperature gradients between the two wells could be beneficial of both wells store water with a higher temperature that the surrounding ambient groundwater. Additionally, the hydraulic heads produced by the wells could be beneficial in counteracting ambient groundwater flow. Therefore, examining the most efficient scenarios of HT-ATES with multiple wells in regions with ambient groundwater flow can be beneficial towards realizing HT-ATES.

5. Conclusion

By the hand of numerical simulations, the impact of ambient groundwater flow on HT-ATES systems in scenarios with the presence of an overlying aquifer was assessed in terms of recovery efficiency and thermal spreading. Depending on the initial impact of density-driven flow, relative efficiency losses due to ambient groundwater flow are either higher or lower than those calculated for LT-ATES systems. However, the trend over R/u, where efficiency losses decrease when going to a larger system or lower *AGF* velocity, is similar to that of LT-ATES. Therefore, the analytical formula of Bloemendal & Hartog 2018 is still applicable to evaluate whether ambient groundwater flow plays a significant role in efficiency losses. In terms of thermal spreading, ambient groundwater flow causes a significant increase in thermal spreading in direction of flow. Increasing the injection volume of a system where ambient groundwater flow is present results in more absolute heat displacement out of the well catchment due to *AGF,* resulting in significantly more horizontal spreading.

The presence of an overlying aquifer causes a considerable increase in vertical upward spreading of heat in HT-ATES systems due to the presence of flow. Density driven flow in the storage aquifer results in more heat to conduct upwards. Subsequently, density-driven flow in the overlying aquifer spreads the heat vertically, resulting in a larger area over which heat may accumulate. Having flow in the overlying aquifer bears no significant effect on the thermal recovery, even in scenarios with relatively flat thermal storage volumes. The flow does reduce the spreading in vertical direction caused due to density-driven flow and increases spreading in the horizontal direction. This induces increased spreading of heat while the overall temperature range decreases. The hypothetical scenarios of having flow in both aquifers have contributed to the understanding of the vertical conduction patterns between the two aquifers. Overall the study has provided a basic understanding of how HT-ATES interplays with site specific hydrogeological conditions and therefore how these must be taken into account when realizing HT-ATES.

References

Anderson, M. P. (2005). Heat as a ground water tracer. *Ground Water*, *43*(6), 951–968. https://doi.org/10.1111/j.1745-6584.2005.00052.x

Bloemendal, M., & Hartog, N. (2018). Analysis of the impact of storage conditions on the thermal recovery efficiency of low-temperature ATES systems. *Geothermics*, *71*(September 2017), 306–319. https://doi.org/10.1016/j.geothermics.2017.10.009

Bloemendal, M., Olsthoorn, T., & van de Ven, F. (2015). Combining climatic and geo-hydrological preconditions as a method to determine world potential for aquifer thermal energy storage. *Science of the Total Environment*, *538*, 621–633. https://doi.org/10.1016/j.scitotenv.2015.07.084

Buscheck, T., Doughty, C., & Fu Tsang, C. (1983). Prediction and Analysis of a Field Experiment on a Multilayered Aquifer Thermal Energy Storage System With Strong Buoyancy Flow. *Water Resources Research*, *19*(NO.5), 1307–1315.

Caljé, R. J. (2010). Furure use of Aquifer Thermal Energy Storage below the historic centre of Amsterdam. *Master Thesis*, (January).

Ceric, A., & Haitjema, H. (2005). On using simple time-of-travel capture zone delineation methods. *Ground Water*, *43*(3), 408–412. https://doi.org/10.1111/j.1745-6584.2005.0035.x

Demirbas, M. F. (2006). Thermal energy storage and phase change materials: an overview. Energy Sources, Part B: Economics, Planning, and Policy, 1(1), 85-95.

Doughty, C., Hellström, G., Tsang, C. F., & Claesson, J. (1982). A dimensionless parameter approach to the thermal behavior of an aquifer thermal energy storage system. *Water Resources Research*, *18*(3), 571–587. https://doi.org/10.1029/WR018i003p00571

Ferguson, G. (2007). Heterogeneity and thermal modeling of ground water. *Ground Water*, *45*(4), 485–490. https://doi.org/10.1111/j.1745-6584.2007.00323.x

Fleuchaus, P., Godschalk, B., Stober, I., & Blum, P. (2018). Worldwide application of aquifer thermal energy storage – A review. *Renewable and Sustainable Energy Reviews*, *94*(July), 861–876. https://doi.org/10.1016/j.rser.2018.06.057

Hasnain, S. M. (1998). Review on sustainable thermal energy storage technologies, part I: Heat storage materials and techniques. *Energy Conversion and Management*, *39*(11), 1127–1138. https://doi.org/10.1016/S0196-8904(98)00025-9

Hecht-Méndez, J., Molina-Giraldo, N., Blum, P., & Bayer, P. (2010). Evaluating MT3DMS for heat transport simulation of closed geothermal systems. *Ground Water*, *48*(5), 741–756. https://doi.org/10.1111/j.1745-6584.2010.00678.x

Hellstrom, G., Tsang, C. F., & Claesson, J. (1979). *Heat storage in aquifers: Buoyancy flow and thermal stratification problems*.

Hesaraki, A., Holmberg, S., & Haghighat, F. (2015). Seasonal thermal energy storage with heat pumps and low temperatures in building projects - A comparative review. *Renewable and Sustainable Energy Reviews*, *43*, 1199–1213. https://doi.org/10.1016/j.rser.2014.12.002

Kabus, F., & Seibt, P. (2000). Aquifer thermal energy storage for the Berlin Reichstag building-new seat of the german parliament. In Proceedings of the World Geothermal Congress (pp. 3611-3615).

Ministry-of-Economic-affairs, 2016. Energieagenda, Naar een CO_2-arme energievoorziening. Ministry of Economic affairs, Den Haag.

Possemiers, M., Huysmans, M., & Batelaan, O. (2014). Influence of Aquifer Thermal Energy Storage on groundwater quality: A review illustrated by seven case studies from Belgium. *Journal of Hydrology: Regional Studies*, *2*, 20-34.

Réveillère, A., Hamm, V., Lesueur, H., Cordier, E., & Goblet, P. (2013). Geothermal contribution to the energy mix of a heating network when using Aquifer Thermal Energy Storage: modeling and application to the Paris basin. Geothermics, 47, 69-79.

RHC, 2013. Renewable Heating & Cooling. European Technology Platform, Brussels Strategic Research and Innovation Agenda for Renewable Heating & Cooling.

Sanner, B., Kabus, F., Seibt, P., & Bartels, J. (2005, April). Underground thermal energy storage for the German Parliament in Berlin, system concept and operational experiences. In Proceedings world geothermal congress (Vol. 1, pp. 1-8).

Sommer, W., Valstar, J., Leusbrock, I., Grotenhuis, T., & Rijnaarts, H. (2015). Optimization and spatial pattern of large-scale aquifer thermal energy storage. *Applied Energy*, *137*, 322–337. https://doi.org/10.1016/j.apenergy.2014.10.019

TNO, 2018. Validate CO2-reductiemodel Nuon warmtenetten 2017, Nederlandse Organisatie voor Toegepast Natuurwetenschappelijk Onderzoek, Delft

UN, 2015. Adoption of the Paris Agreement. United Nations, Framework Convention on Climate Change, Paris.

Wesselink, M., Liu, W., Koornneef, J., & van den Broek, M. (2018). Conceptual market potential framework of high temperature aquifer thermal energy storage - A case study in the Netherlands. *Energy*, *147*, 477–489. https://doi.org/10.1016/j.energy.2018.01.072

Appendix

Appendix 1.1

	Injection temperature 30 °C					Injection temperature 90 °C				
Injection Volume [m³]	**100.000**	**200.000**	**400.000**	**600.000**	**800.000**	**100.000**	**200.000**	**400.000**	**600.000**	**800.000**
No *AGF*										
No Density	0.818	0.828	0.840	0.845	0.849	0.818	0.828	0.840	0.845	0.849
Density	0.810	0.828	0.840	0.845	0.849	0.647	0.725	0.794	0.816	0.827
Flow storage aqf. [m/yr]										
25	0.777	0.808	0.829	0.838	0.843	0.632	0.720	0.782	0.807	0.820
50	0.715	0.767	0.803	0.818	0.827	0.577	0.678	0.752	0.783	0.800
100	0.592	0.675	0.737	0.767	0.784	0.452	0.569	0.672	0.717	0.743
Flow overlying aqf. [m/yr]										
25	0.770	0.803	0.826	0.835	0.841	0.627	0.716	0.779	0.811	0.818
50	0.704	0.756	0.795	0.812	0.822	0.567	0.678	0.744	0.784	0.794
100	0.578	0.661	0.725	0.754	0.772	0.437	0.553	0.659	0.705	0.732
Flow both aqfs. [m/yr]										
25	0.807	0.825	0.839	0.844	0.848	0.655	0.736	0.793	0.815	0.826
50	0.803	0.822	0.836	0.842	0.846	0.653	0.735	0.791	0.813	0.825
100	0.798	0.817	0.832	0.838	0.843	0.636	0.715	0.787	0.810	0.822

Table 5 All recovery efficiencies calculated of the standard scenarios modelled. The efficiencies are of the calculated over the last full operational year

Appendix 1.2

	Injection temperature 90 ˚C		
Thickness middle aqd. [m]	1	5	15
No flow	0.800	0.794	0.784
Flow storage aqf. [m/yr]			
25	0.788	0.782	0.774
50	0.757	0.752	0.747
100	0.675	0.672	0.673
Flow overlying aqf. [m/yr]			
25	0.788	0.779	0.765
50	0.756	0.744	0.726
100	0.672	0.659	0.641
Flow both aqfs. [m/yr]			
25	0.800	0.793	0.781
50	0.799	0.791	0.776
100	0.799	0.787	0.766

Table 6 Recovery efficiencies of the scenarios modelled with a different middle aquitard thickness. The efficiencies are of the calculated over the last full operational year

Appendix 2

	V_{str} = 1000 m³			V_{str} = 8000 m³		
Days	**R_h**	**R_{th}**	**Dispersivity**	**R_h**	**R_{th}**	**Dispersivity**
0	0	0	0	0	0	0
7	6.21	3.47	1.65	17.60	9.83	4.68
14	10.73	5.99	1.20	30.40	16.98	3.40
21	15.12	8.45	1.17	42.83	23.92	3.31
28	19.44	10.86	1.15	55.02	30.73	3.24
35	23.66	13.22	1.12	66.98	37.41	3.18
42	27.81	15.53	1.10	78.67	43.93	3.11
49	31.83	17.78	1.07	90.05	50.29	3.03
56	35.74	19.96	1.04	101.11	56.47	2.94
63	39.52	22.07	1.01	111.79	62.43	2.84
70	43.15	24.10	0.97	122.05	68.17	2.73
77	46.63	26.04	0.92	131.87	73.65	2.61
84	49.93	27.88	0.88	141.20	78.86	2.48
91	53.04	29.62	0.83	150.02	83.78	2.34
98	55.96	31.26	0.78	158.28	88.40	2.20
105	58.69	32.78	0.72	165.97	92.69	2.04
112	61.19	34.17	0.67	173.05	96.65	1.88
119	63.47	35.45	0.61	179.50	100.25	1.72
126	65.52	36.59	0.55	185.29	103.48	1.54
133	67.33	37.60	0.48	190.41	106.34	1.36
140	68.89	38.48	0.42	194.83	108.81	1.18
147	70.20	39.21	0.35	198.53	110.88	0.99
154	71.25	39.80	0.28	201.52	112.54	0.79
161	72.05	40.24	0.21	203.76	113.80	0.60
168	72.58	40.53	0.14	205.26	114.64	0.40
175	72.84	40.68	0.07	206.02	115.06	0.20

Table 7 The hydraulic radius, thermal radius and dispersivity only due to dispersion calculated for the smallest system modelled (V_{str} = 100.000 m³) and largest system modelled (V_{str} = 800.000 m³)